



Repositorio Institucional de la Universidad Autónoma de Madrid

<https://repositorio.uam.es>

Esta es la **versión de autor** del artículo publicado en:

This is an **author produced version** of a paper published in:

Monthly Notices of Royal Astronomical Society 446.3 (2015): 2837-2860

DOI: 10.1093/mnras/stu2295

Copyright: © 2015 The Authors: Published by Oxford University Press
on behalf of the Royal Astronomical Society

El acceso a la versión del editor puede requerir la suscripción del recurso
Access to the published version may require subscription

Dissecting galactic bulges in space and time I: the importance of early formation scenarios vs. secular evolution

M. K. Seidel^{1,2*}, R. Cacho³, T. Ruiz-Lara^{4,5}, J. Falcón-Barroso^{1,2}, I. Pérez^{4,5},
P. Sánchez-Blázquez⁶, F. P. A. Vogt⁷, M. Ness⁸, K. Freeman⁷ and S. Aniyani^{7,9}

¹*Instituto de Astrofísica de Canarias, E-38200 La Laguna, Tenerife, Spain*

²*Departamento de Astrofísica, Universidad de La Laguna, E-38205 La Laguna, Tenerife, Spain*

³*Dpto. de Astrofísica y CC. de la Atmósfera, Universidad Complutense de Madrid, Spain*

⁴*Dpto. de Física Teórica y del Cosmos, Universidad de Granada, Facultad de Ciencias (Edificio Mecenas), 18071 Granada, Spain*

⁵*Instituto Universitario Carlos I de Física Teórica y Computacional, Universidad de Granada, 18071 Granada, Spain*

⁶*Dpto. de Física Teórica, Universidad Autónoma de Madrid, E-28049 Cantoblanco, Spain*

⁷*Research School of Astronomy and Astrophysics, Australian National University, Canberra, ACT 2611, Australia*

⁸*Max-Planck-Institut für Astronomie, Königstuhl 17, D-69117 Heidelberg, Germany*

⁹*European Southern Observatory, Karl-Schwarzschild-Str. 2, 85748 Garching, Germany*

13 November 2014

ABSTRACT

The details of bulge formation via collapse, mergers, secular processes or their interplay remain unresolved. To start answering this question and quantify the importance of distinct mechanisms, we mapped a sample of three galactic bulges using data from the integral field spectrograph WiFeS on the ANU 2.3m telescope in Siding Spring Observatory. Its high resolution gratings ($R \sim 7000$) allow us to present a detailed kinematic and stellar population analysis of their inner structures with classical and novel techniques. The comparison of those techniques calls for the necessity of inversion algorithms in order to understand complex substructures and separate populations. We use line-strength indices to derive SSP-equivalent ages and metallicities. Additionally, we use full spectral fitting methods, here the code `STECKMAP`, to extract their star formation histories. The high quality of our data allows us to study the 2D distribution of different stellar populations (i.e. young, intermediate, and old). We can identify their dominant populations based on these age-discriminated 2D light and mass contribution. In all galactic bulges studied, at least 50% of the stellar mass already existed 12 Gyrs ago, more than currently predicted by simulations. A younger component (age between ~ 1 to ~ 8 Gyrs) is also prominent and its present day distribution seems to be affected much more strongly by morphological structures, especially bars, than the older one. This in-depth analysis of the three bulges supports the notion of increasing complexity in their evolution, likely to be found in numerous bulge structures if studied at this level of detail, which cannot be achieved by mergers alone and require a non-negligible contribution of secular evolution.

Key words: galaxies: bulges, galaxies: evolution, galaxies: formation, galaxies: kinematics and dynamics, galaxies: stellar content, techniques: spectroscopic

1 INTRODUCTION

Galactic bulges, considered as a deviation from the exponential profile in the centre of galaxies, are one of the keys to study galaxy formation and evolution processes, and yet many details of their origin remain unresolved. The different formation scenarios brought forward during the last decades describe mainly two bulge types: classical merger-driven bulges and pseudobulges resulting from secular and/or internal evolution scenarios (e.g. Kormendy & Kennicutt 2004 and references therein). Increasingly detailed studies in the

last years have however revealed the presence of rich substructures within those bulges which cannot be fully attributed to one common evolution scenario. Athanassoula (2005) redefined the classes based on numerical simulations into: *classical bulges* being results of mergers or monolithic collapse, *boxy/peanut bulges* formed via the natural evolution of barred galaxies (see also Combes & Sanders 1981) and *disc-like bulges* resulting from the inflow of gas to the centre-most parts triggering star formation. The latter two bulge types are both results from secular processes within the host galaxy, so that the division by physical origin remains to be i) classical and ii) secularly evolved bulges.

* E-mail: mseidel@iac.es

Pioneering research and recent discoveries show a variety

Table 1. Galaxy sample properties. The columns show the following: (1) NGC number; (2) Hubble type (RC3; de Vaucouleurs et al. 1995); (3) - (6) J2000 coordinates (right ascension, declination), absolute B -band magnitude and inclination (taken from HyperLeda); (7) and (8) bulge effective radius and bulge Sérsic index (taken from Weinzirl et al. 2009); (9) - (13) $H\beta$ and Mgb line strength indices in \AA and mag as determined from our data in a central circular aperture of radius of 1.5 arcsec.

Galaxy	RC3 Type	RA	Dec	M_B	incl.	Bulge r_e	Bulge n	σ_{cen}	$H\beta$	$H\beta$	Mgb	Mgb
(1)	(2)	(h, m, s)	(d, m, s)	(mag)	(deg)	(arcsec)	(8)	(km s^{-1})	(\AA)	(mag)	(\AA)	(mag)
NGC 5701	(R)SB(rs)0/a	14 39 11.1	+05 21 49	-19.99	40.6	11.13	2.41	112	3.82	0.136	1.95	0.076
NGC 6753	(R)SA(r)b	19 11 23.6	-57 02 58	-21.65	30.1	1.50	0.94	214	4.80	0.174	1.60	0.062
NGC 7552	(R')SB(s)ab	23 16 10.8	-42 35 05	-20.52	23.6	2.70	0.64	89	1.20	0.041	5.00	0.208

of different bulges with and without rich substructures hinting to secular evolution - not only bar-driven. Disentangling these different components can be resolved in different ways: (i) Photometric observations allow us to study the morphological features and substructures, e.g. bulge-disc decomposition, through their light distribution (e.g. de Souza, Gadotti & dos Anjos 2004; Laurikainen et al. 2007) and the derived broad-band colours can already give us an idea of the present stellar populations (e.g. Bell & de Jong 2000; MacArthur et al. 2004; Gadotti & de Souza 2006; Muñoz-Mateos et al. 2007; Roediger et al. 2012); abundant photometric studies also relate star formation rates and stellar masses to distinct bulge types (e.g. Fisher & Drory 2011) (ii) Spectroscopic observations provide us with the kinematic properties (e.g. Falcón-Barroso et al. 2006; Ganda et al. 2006) and distribution of stellar populations in these galaxies (e.g. Trager et al. 2000; Kuntschner 2000; MacArthur, González & Courteau 2009; Sánchez-Blázquez et al. 2011).

While resolving stellar populations would be ideal (instead of integrated light), this is limited to only a few galaxies within the Local Group (e.g. Tolstoy, Hill & Tosi 2009; Frebel et al. 2010). Therefore integrated spectra and especially colours are usually employed. Thanks to technical developments during the last decade, the separation of stellar and gas contributions in the spectra could be achieved (e.g. Sarzi et al. 2006) and due to better instrumentation, fainter (sub-)structures could be revealed (e.g. MacArthur, González & Courteau 2009; Pérez & Sánchez-Blázquez 2011; Sánchez-Blázquez et al. 2011). Furthermore, major developments in stellar population analysis techniques coupled with the improved calibration and extension of spectral stellar libraries (e.g., STELIB, Le Borgne et al. 2003; MILES, Sánchez-Blázquez et al. 2006b; Indo-US, Valdes et al. 2004; CaT, Cenarro et al. 2001a,b) have pushed stellar population analyses forward.

Early-type galaxies and classical bulges were once assumed to be characterised by single stellar populations whose stars formed long ago on short timescales (e.g. Hernquist 1990; Trager et al. 2000). In fact, first bulge studies focused on early-types (to avoid the gas) and compared bulges to elliptical galaxies (e.g. Sansom, Proctor & Reid 1998; Proctor & Sansom 2002). However, modern detailed population analyses of bulge systems (e.g. Moorthy & Holtzman 2006; Jablonka, Gorgas & Goudfrooij 2007; Morelli et al. 2008), largely based on well-resolved spectroscopy, have revealed a more complex picture of star formation history occurring at both early and later times. Especially the analysis of more complex secularly driven structures which formed over longer periods had to be revised. For this analysis, inversion algorithms (e.g. STARLIGHT: Cid Fernandes et al. 2005; STECKMAP: Ocvirk et al. 2006a,b; FIT3D: Sánchez et al. 2006; ULySS: Koleva et al. 2009) were developed to perform full-spectral fitting of the data comparing it with a set of synthetic model spectra for a range of ages and metallicities.

Only very few studies have investigated galactic bulges in this great detail up to date and only few have used integral-field spectroscopy (e.g. Ganda et al. 2007; Joachim, Roškar & Debattista 2012; Sánchez-Blázquez et al. 2014). Ocvirk, Peletier & Lançon (2008) demonstrated that a young and cold stellar population could be distinguished from an old and hot bulge using age - line-of-sight-velocity-distribution (LOSVD) diagrams. More recent attempts in the literature to achieve similar goals (using different techniques) are very scarce and usually restricted to very few, well-known multiple component systems (e.g. van der Laan et al. 2013b; Coccato et al. 2011, 2013; Johnston et al. 2013). Despite great progress, especially with the advent of large spectroscopic surveys (e.g. ATLAS3D, Cappellari et al. 2011), we are still far from understanding galactic bulges and their subcomponents, both kinematically and from the stellar population point of view.

In this paper, we present an in-depth study of three fundamentally different bulges using the WiFeS integral field spectrograph on the ANU 2.3m telescope in Siding Spring Observatory. The combination of its large spectral range, high spectral resolution gratings and sufficiently large field of view allows us to explore the entire range of tools to derive stellar and gas kinematics, but also their stellar population content. In Sec. 2 we will describe our target selection and observations, while Sec. 3 provides details of the data reduction process. The methods employed to perform the different analyses are described in Sec. 4. Section 5 presents the results for the stellar and ionised-gas kinematics. Section 6 introduces the different stellar population results using the classical indices method and the novel technique via full-spectral fitting. These results are discussed in Sec. 7. Finally, Sec. 8 summarizes our main findings.

2 SAMPLE OBSERVATIONS

2.1 Target selection

The target selection aimed at providing galaxies with distinct properties and level of morphological substructure seen in the photometry in their inner regions in order to quantify the importance of the different stellar populations present in each system. Therefore we chose galaxies with three distinct galactic bulges in barred, unbarred and ringed galaxies, spanning a very different level of complexity in stellar populations based on the literature. We selected bright, prominent bulges to maximize the quality of the data while reducing the required observing time. The sample was selected from the Carnegie-Irvine Galaxy Survey (Ho et al. 2011) and the catalogue of inner disks and rings (Erwin & Sparke 2002), with extensive ancillary photometric decompositions (Weinzirl et al. 2009; Li et al. 2011). Detailed descriptions of each galaxy can be found in the Appendix A. Despite the obvious limitations of a sample of only

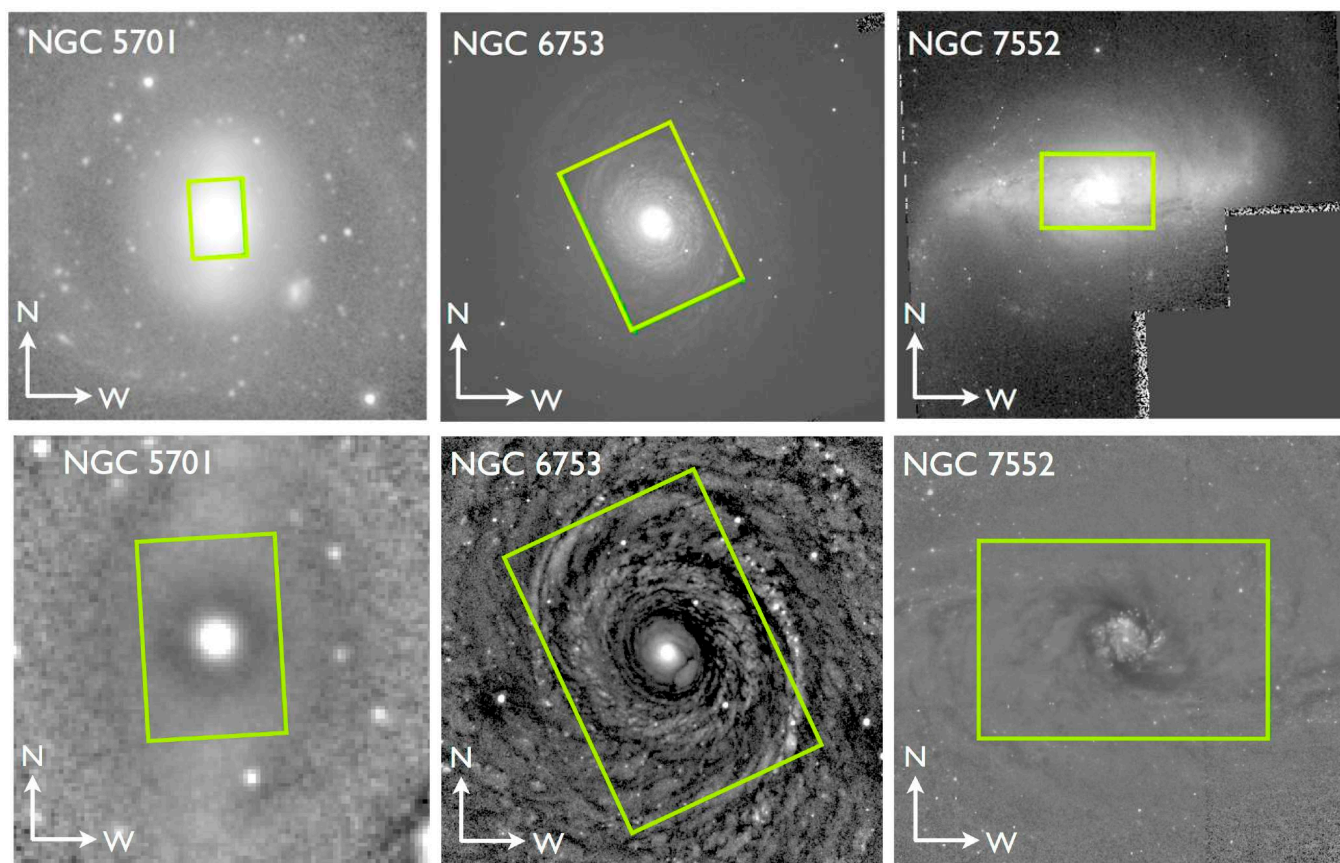


Figure 1. (Top row) Sample of galaxies observed with the WiFeS spectrograph. Spitzer $3.6\mu\text{m}$ imaging from the $S^4\text{G}$ survey is shown for NGC 5701 (left), while HST imaging in the F814W filter is presented for NGC 6753 (middle) and NGC 7552 (right). The green rectangle marks the footprint of the WiFeS FoV (25×38 arcsec). (Bottom row) Unsharp mask images for our sample of galaxies. See §2.2 for details.

three galaxies, this pilot study allows us to compare these systems and still detect significant similarities, see e.g. §7.2, helping us to understand common fundamental formation and evolution mechanisms throughout bulges in disk galaxies.

We retrieved *Hubble Space Telescope* (HST) Wide Field Planetary Camera 2 archival data, in the F814W filter, for NGC 6753 and NGC 7552 from the Hubble Legacy Archive¹. For NGC 5701, we used $S^4\text{G}$ imaging² (Sheth et al. 2010) given that no HST data were available (see Fig. 1). The basic characteristics, taken from HyperLeda³, are listed in Table 1. The table also contains bulge characteristics determined by Weinzirl et al. (2009) via two-dimensional surface brightness decomposition as well as central (circular aperture of 1.5 arcsec) velocity dispersions and line-strength values extracted from our own analysis.

2.2 Level of substructure from unsharp masking

In our galaxies certain substructures are already evident from the photometric images shown in the upper row of Fig. 1. Nevertheless, we have produced unsharp masked images, following Erwin (2004)

and Lisker et al. (2006), to reveal any small-scale structures or structures with no radial symmetries that may be present. This method relies on the presence of a smooth and symmetric overall light distribution which can be modeled by the `gauss` task of IRAF⁴ (Tody 1993). Then the original image can be divided by the smooth model to obtain the unsharp mask. For NGC 6753 and NGC 7552, we used a value of $\sigma_{\text{mask}} = 20$ for the Gaussian convolution and $\sigma_{\text{mask}} = 5$ for NGC 5701. We determined the ellipticity and PA values from our own reconstructed images (i.e. intensity images extracted from WiFeS datacubes). The results are presented in the bottom row of Fig. 1. The different substructures stand out very clearly. NGC 5701 shows a rather smooth distribution with a strong central feature. The rectangle indicating the WiFeS FoV exacerbates the proper visualization of its large scale bar, which can be seen rather faint here. NGC 6753 also exhibits a prominent central component, but with significant flocculent spiral structure throughout the FoV, but mainly concentrated in the inner ring. In NGC 7552, the dust lanes are very evident, along with the bright circumnuclear ring with star forming regions of different intensities.

¹ <http://hla.stsci.edu>, based on observations made with the NASA/ESA HST, obtained from the European Southern Observatory (ESO)/ST-ECF Science Archive Facility.

² <http://irsa.ipac.caltech.edu/data/SPITZER/S4G/>

³ <http://leda.univ-lyon1.fr/>

⁴ IRAF is distributed by the National Optical Astronomy Observatory, which is operated by the Association of Universities for Research in Astronomy, Inc., under cooperative agreement with the National Science Foundation.

2.3 Observations

The observations were taken in July and September 2013 at the 2.3m telescope at Siding Spring Observatory (SSO) in Australia. We used the WiFeS IFU which provides a 38×25 arcsec² field-of-view with 1×1 arcsec per spatial element. It was commissioned in May 2009 and its detailed description can be found in Dopita et al. (2007, 2010). The instrument’s dichroic allows observations with two gratings simultaneously. Using the RT615 dichroic, we chose the two high resolution gratings B7000 and I7000. The B7000 grating results in a wavelength coverage of 4180 to 5580 Å with a spectral resolution (σ) of 43 km/s, more details for our data in §3. The I7000 grating ranging from 6800 to 8900 Å supplies the information on the Calcium triplet region. The good instrumental resolution allowed us to measure the lowest expected velocity dispersions while the large spectral coverage still ensures a meaningful full-spectral fitting analysis.

The central surface brightness for the bulges in our sample is $\mu \simeq 18$ mag arcsec⁻² (Li et al. 2011). A minimum S/N per resolution element of $S/N \approx 20$ is required to characterize the kinematics and stellar populations of each separate stellar components (e.g. Johnston et al. 2013). We aimed at 4 hour integration times for each galaxy in order to achieve that S/N and still maintain the maximum spatial sampling provided by the instrument (i.e. 1×1 arcsec). We obtained 4800 seconds (4×20 min exposures) each for NGC 5701 and NGC 7552 and 14400 seconds (12×20 min exposures) for NGC 6753. Although we lost observation time on the first two targets due to weather conditions, their data are still very useful, just with somewhat coarser binning. The average seeing was around 1.5 arcsec, September being slightly better than July.

We observed one single pointing per galaxy centred on the bulge dominated region (see Fig. 1). Nonetheless, the large FoV allowed us to reach disk dominated regions. We took calibration frames (bias, flats and arc) before dawn and after dusk, and sky flats during twilight. The observational strategy was to “point-and-stare”, i.e. to observe in blocks of object–sky–object, calibration frames and calibration stars. This strategy was designed to have sky and calibrations near each science frame to avoid temporal effects. We decided to adopt this method rather than the nod-and-shuffle method available for WiFeS since it maximized the exposure time on the science frames. Instead of taking the same amount of time on the sky and object frames, we decided to increase the time spent on the object frames to increase the signal, and at the expense of slightly larger noise level (i.e. increase by the square root of 2).

3 DATA REDUCTION

We reduced and calibrated our data using the new pipeline designed for this instrument, PyWiFeS⁵. The pipeline performs a typical reduction on each single WiFeS frame which consists of 25 slit spectra being 1 arcsec wide and 38 arcsec long. The reduction includes bias subtraction, flatfielding, distortion correction, wavelength calibration, sky (and additional telluric correction for the red arm) subtraction, sensitivity curve correction and datacube generation. Details can be found in Childress et al. (2014).

For the wavelength calibration of our frames, we had to devise a non-standard solution. This was done using neon and argon arc lamp spectra which were taken close to the science exposures during the entire night. Since this lamp had not been used before

with the B7000 and I7000 high resolution gratings, we created our own reference files from the arc lamp measurements and calibrated them with the line values given, relative to air, on the NIST webpage⁶. We ensured the accuracy of this calibration by reducing arc lamp spectra as well as sky frames and checking the position of the arc and sky lines. This resulted in an uncertainty of $\Delta \approx 0.1$ Å. The datacubes were flux calibrated with the help of flux standard stars observed: HIP71453, EG131 and Feige110, to achieve a relative flux calibration. For the red-arm spectra, the removal of telluric lines was achieved using observations of featureless white dwarfs, taken close to the science frames and at similar air masses as the object.

The data reduction is run separately for the blue and red arm frames. After finding the offsets, we use the *iraf imcombine* routine to merge the individual cubes to a single datacube sampled to a common spatial grid. The blue spectra span from 4100 Å to 5500 Å with a spectral sampling of 0.347 Å per pixel and a spectral resolution (Full Width Half Maximum, FWHM) of $FWHM \approx 0.9$ Å. The red spectra cover the range from 6808 Å to 8930 Å with a spectral sampling of 0.5665 Å per pixel and a spectral resolution of $FWHM \approx 1.5$ Å. In both cases the spectral resolution was not constant along the frame and therefore we convolved the spectra in each case to the highest measured FWHM values, setting the final spectral resolution to $FWHM \approx 1.0$ Å and $FWHM \approx 1.6$ Å for the blue and red setups respectively.

4 METHODS

In our analysis of kinematics and stellar populations, we adopted a Voronoi binning scheme (Cappellari & Copin 2003) to reach the desired S/N levels. We chose to bin our data for NGC 5701 and NGC 7552 to $S/N \approx 20$ and for NGC 6753 to $S/N \approx 40$. This choice ensures a meaningful analysis while maximizing the spatial sampling, which is important to resolve substructures present in our maps. The extension of the field is the WiFeS FoV, however bins of too low signal (less than $S/N=3$) have been left out.

4.1 Stellar kinematics

We extracted the stellar kinematics from the blue and red arm separately. For simplicity, we present the results from the blue spectra only. Both sets of maps agree within the uncertainties. We used the pPXF –penalized pixel fitting– code developed by Cappellari & Emsellem (2004) to extract the stellar kinematics. The routine fits each galaxy spectrum with a combination of template spectra. We used a subset of PEGASE high resolution model spectra PEGASE-HR with $R \approx 10000$ (Le Borgne et al. 2004) spanning a wide range of ages and metallicities in order to minimize the impact of template mismatch. Before the fitting process, we matched the spectral resolution of those models to that of our data. pPXF uses a Gauss-Hermite parametrization (Gerhard 1993; van der Marel & Franx 1993) to describe the LOSVD and thus allows the measurement of the velocity (V), velocity dispersion (σ) and higher order Gauss-Hermite moments (h_3 and h_4).

⁵ <http://www.mso.anu.edu.au/mjc/wifes.html>

⁶ <http://www.nist.gov/pml/data/index.cfm>

4.2 Ionised gas extraction

The measurement of the stellar population parameters requires the removal of the ionised emission present in the spectra. This is particularly important in the Balmer lines (i.e. $H\gamma$ and $H\beta$) present in our wavelength range, which are the key features determining the age of the stellar population.

We use the Gas AND Absorption Line Fitting (GANDALF) package by Sarzi et al. (2006) and Falcón-Barroso et al. (2006) to obtain the ionised-gas distribution and kinematics. The emission lines are treated as additional Gaussian templates on top of the stellar continuum and the code iteratively looks for the best match of their velocities and velocity dispersions. For the blue-arm spectra, we could measure the following emission lines: $H\gamma\lambda 4341$, $H\beta\lambda 4861$ and the doublets $[OIII]\lambda\lambda 4959, 5007$ and $[Ni]\lambda\lambda 5200, 5202$. We tied spectral lines kinematically as it helps constraining the parameters for GANDALF and leaving them free gave matching results. We always chose the strongest lines in each case: in NGC 5701, we fixed the kinematics of the emission lines to the $[OIII]$ doublet and in NGC 6753 and NGC 7552, we fixed the emission line kinematics to the $H\beta$ line instead. We furthermore imposed known relative flux relations to constrain the freedom of the lines during the fitting process, namely $F(H\gamma) = 0.469 \cdot F(H\beta)$ and $F([OIII]_{4959}) = 0.350 \cdot F([OIII]_{5007})$.

We thus used our results from GANDALF to *clean* the spectra of our galaxies and produce emission-line-free datacubes for our stellar population analysis.

4.3 Stellar populations via line-strength indices

The comparison of absorption line-strength indices measured on observed spectra with those computed with single stellar populations (SSP) models is the classical approach to derive stellar population parameters from integrated spectra (e.g. Faber 1973; Davies, Sadler & Peletier 1993; Worthey et al. 1994; Vazdekis 1999; Thomas et al. 2005; Sánchez-Blázquez et al. 2006a; Kuntschner et al. 2006; MacArthur, González & Courteau 2009). Lick/IDS indices are the most commonly used to probe the luminosity-weighted age, metallicity and abundance ratios of specific elements.

We started our analysis with this method by relating our index measurements to the MILES model predictions (Vazdekis et al. 2010). We obtained the absorption line strengths in the Line Index System at 8.4 \AA (LIS- 8.4\AA) (Trager et al. 1998; Vazdekis et al. 2010). This approach allows us to avoid the intrinsic uncertainties associated with the popular Lick/IDS system. In this study, we measured the following indices from the blue grating: Ca4227, G4300, $H\gamma A$, $H\gamma F$, Fe4383, Ca4455, Fe4531, Fe4668, $H\beta$, $H\beta_o$ (Cervantes & Vazdekis 2009), Fe5015, Fe5270, Mgb, Fe5270, Fe5335 and Fe5406. From the red grating, we also determined indices following Cenarro et al. (2001a): CaT, CaT*, and PaT with Ca1($\lambda\lambda 8484.0-8515.0$), Ca2($\lambda\lambda 8522.0-8562.0$), Ca3($\lambda\lambda 8642.0-8682.0$), Pa1($\lambda\lambda 8461.0-8474.0$), Pa2($\lambda\lambda 8577.0-8619.0$) and Pa3($\lambda\lambda 8730.0-8772.0$).

While we only made use of some of them to derive our results, we provide a summary of all maps for each galaxy in both gratings in the appendix. In the particular case of NGC 6753 the central spectra are intrinsically more broaden than 8.4 \AA . A few central spectra exhibit an average broadening of $\approx 9 \text{ \AA}$. This results in a shift of $\approx 0.02 \text{ \AA}$ in $H\beta$ and $\approx 0.05 \text{ \AA}$ in Mgb. This would correspond to a difference of 1.5 Gyr from our measured value and it is well within our uncertainties. Given the small effect, and for simplicity,

we chose to not convolute the data further and use the models at 8.4 \AA .

In Sect. 6 we use the $H\beta_o$, Mgb, Fe5270 and Fe5335 index maps to determine the stellar population parameters. We specifically combine the Mgb, Fe5270 and Fe5335 indices to obtain the $[MgFe]'$ index (e.g. Thomas, Maraston & Bender 2003), as it is almost insensitive to $[Mg/Fe]$ variations. We then use the `rmodel`⁷ code (Cardiel et al. 2003) to compute the mean luminosity-weighted age and metallicity. In Fig. 5, we show the index-index diagrams for our three galaxies with the MILES SSP models for different ages and metallicities overlaid. Throughout this work we assume a Kroupa initial mass function (IMF, Kroupa 2001).

The representation of stellar populations of a galaxy by a SSP is an oversimplification for spiral galaxies. It is for this reason that this method is mostly used in systems where we can assume that the locally averaged metallicity and age do not vary very much across the galaxy (e.g. ellipticals). The errors when representing the local stellar population by an SSP are then the same everywhere (Peletier et al. 2007). While we do not expect a single stellar population in many regions of our sample of bulges, this classical approach provides luminosity-weighted population parameters that are useful to contrast with the literature of similar objects.

4.4 Stellar populations via full-spectral fitting techniques

There are several inversion algorithms in the literature (e.g. Cid Fernandes et al. 2005; Koleva et al. 2009) whose main goal is the reconstruction of the stellar content from an observed spectrum. Full-spectral fitting techniques allow us to maximize the information encoded in a spectrum as they use the entire wavelength range and they are not limited to some specific absorption features (e.g. line-strength indices).

STECKMAP⁸ (Stellar Content and Kinematics via Maximum A Posteriori likelihood, Ocvirk et al. 2006a,b) is a full-spectral fitting code that uses a Bayesian method to simultaneously recover the stellar kinematics and the stellar properties via a maximum a posteriori algorithm. It is non-parametric so it provides properties such as the stellar age distribution (SAD) with minimal constraints on their shape. In addition, the ill-conditioning of the inversion is taken into account through explicit regularization.

In practice, the code determines a linear combination of single stellar population models trying to reproduce the observed spectrum projected onto a temporal sequence of these SSP models. The weights used for the linear combination give the SSP fractions and create the according star formation history associated to the spectrum. Thus, the code does not take any a priori assumption to create the SFHs apart from imposing a smooth solution for the unknown parameters, namely the stellar age distribution, the age-metallicity relation and the line-of-sight velocity distributions or broadening function, which is supposed to avoid un-physical solutions. To achieve this, the code uses certain smoothing parameters whose choice is important, but not sufficiently enough to significantly influence the overall outcome (i.e. main features) of the SFHs, as well as the derived mean values of ages and metallicities. This has been tested in many former works, (e.g. Ocvirk et al. 2006a,b; Ocvirk, Peletier & Lançon 2008; Koleva et al. 2008; Sánchez-Blázquez et al. 2011; Koleva et al. 2011; Sánchez-Blázquez et al. 2014).

For this work, we use the emission-cleaned spectra coming

⁷ <http://www.ucm.es/info/Astrof/software/rmodel/rmodel.html>

⁸ <http://astro.u-strasbg.fr/?ocvirk/>

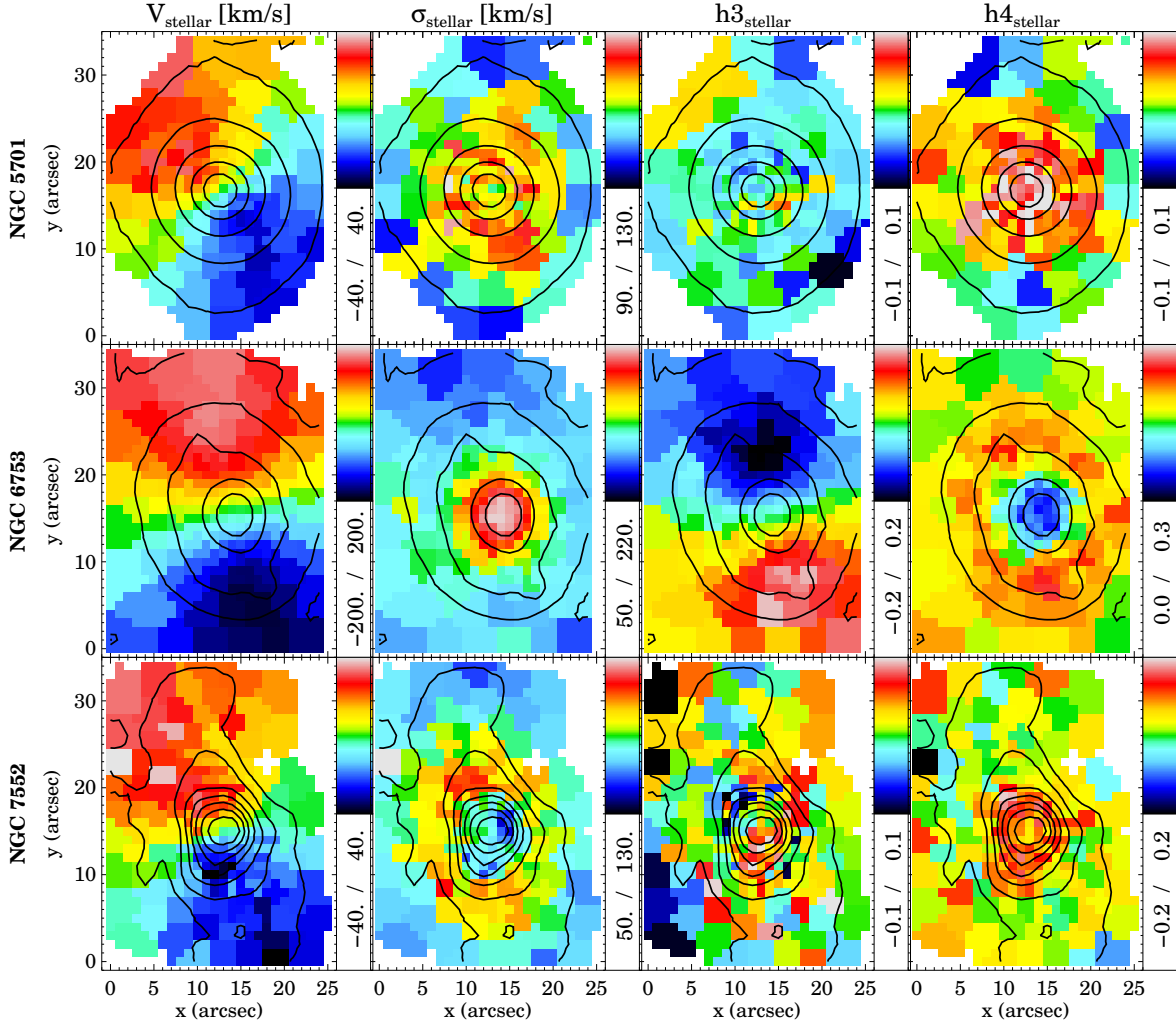


Figure 2. Stellar kinematic maps for all three galaxies, from top to bottom: NGC 5701, NGC 6753 and NGC 7552. For each one, the four panels show stellar velocity, stellar velocity dispersion, h_3 and h_4 moments. The colour bars on the side each indicate the range of the parameter measured. The isophotes shown are derived from the WiFeS cube reconstructed intensities and are equally spaced in stdpf of 0.5 magnitudes.

from the `GANDALF` analysis following the same Voronoi scheme outlined above. We shift the spectra to rest frame according to the stellar velocity (see Sec. 4.1) and broadened them to 8.4 \AA . We fix the stellar kinematics and fit exclusively for the stellar content in order to avoid the metallicity-velocity dispersion degeneracy reported by Sánchez-Blázquez et al. (2011).

As in the previous section, we use the MILES models as the reference templates with the following range of ages and metallicities: 63 Myrs to 17.8 Gyr and $-2.32 < [Z/H] < +0.2$ respectively. We also keep using the Kroupa Universal IMF. The chosen age range can obviously lead to outputs of ages older than the age of the Universe, but in line with globular cluster ages. Several former studies have investigated this zero point problem (e.g. Vazdekis et al. 2001; Schiavon et al. 2002; Vazdekis et al. 2010; Maraston & Strömbäck 2011) and in order to not artificially bias our outcome, we use the entire range of models available, which is also usually done in SP studies.

Once we obtain the star formation history of a given spectrum, we compute the luminosity- (L) and mass- (M) weighted age and metallicity (both represented by q) as follows:

$$\langle q \rangle_M = \sum_i \text{mass}(i) q_i / \sum_i \text{mass}(i), \quad (1)$$

$$\langle q \rangle_L = \sum_i \text{flux}(i) q_i / \sum_i \text{flux}(i). \quad (2)$$

In order to obtain the value of metallicity with respect to solar metallicity $Z_\odot=0.02$ we use:

$$[M/H]_L = -2.5 \log_{10}(Z_L/Z_\odot) \quad (3)$$

$$[M/H]_M = -2.5 \log_{10}(Z_M/Z_\odot) \quad (4)$$

The comparison of the stellar properties from the line-strength indices and the full-spectral fitting will allow us to better understand the limitations of the classical method, i.e. assess the two-fold bias of the indices results proposed by Serra & Trager (2007).

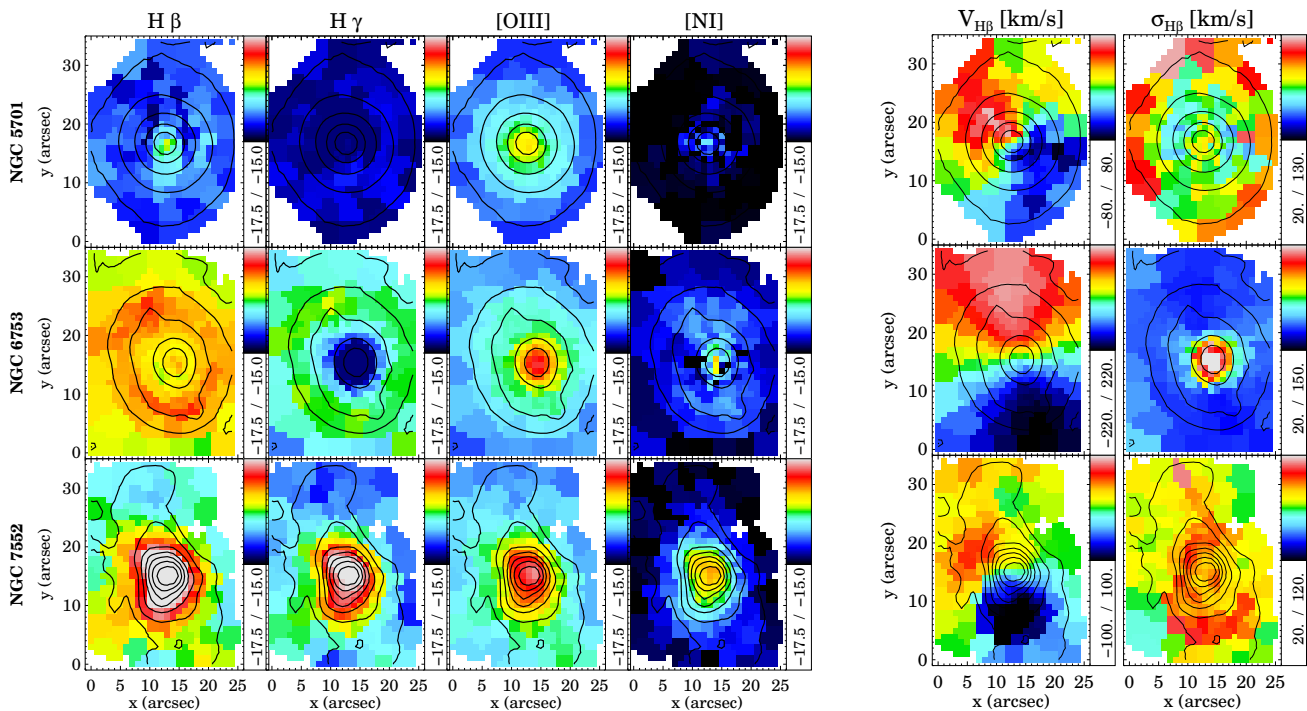


Figure 3. Gas fluxes and velocities for all three galaxies in our sample. The left four columns show the gas intensities, while we present the kinematics on the right: ionised gas rotation velocity and velocity dispersion. Each row represents one galaxy, as indicated on the left hand side. NGC 7552 has a cross of bad pixels on the right (white cross). Fluxes of the emission lines is given in $\text{erg s}^{-1} \text{cm}^{-2} \text{arcsec}^{-2}$ and in a logarithmic scale.

5 KINEMATIC PROPERTIES

Figures 2 and 3 present maps of the absorption and emission-line distribution and kinematics of the three galaxies in our sample. Overlaid in all maps, we show the isophotes of the total intensity reconstructed from the WiFeS spectra (in mag/arcsec^2 with an arbitrary zero point) equally spaced in intervals of 0.5 magnitudes (detailed maps are collected in Appendix E). Here, we concentrate on an overview of the general kinematic trends and results observed.

5.1 Stellar kinematics

NGC 5701 shows a misalignment between the galaxy’s main photometric axis and the bar. The isophotes also indicate that the bar angle is clearly misaligned with respect to the major kinematic axis. The maximum absolute rotation values reach up to 40 km s^{-1} within our FoV. The velocity dispersion is higher in the central parts (110 km s^{-1}) and drops down to 95 km s^{-1} at the edges of the FoV. The highest σ values are not found exactly in the centre, but offset by $\sim 5 \text{ arcsec}$, hence presenting a central σ -drop. The h_3 map reveals some level of anti-correlation in the central parts with the velocity map. This finding is consistent with the elevated h_4 values in the centre. We expect a dominant bulge in this region (Weinzirl et al. 2009), but also weak nuclear spiral arms Erwin & Sparke (2002) which could explain the non-zero h_3 and h_4 values obtained.

In NGC 6753, the photometric and kinematic axes appear to be aligned. This galaxy displays an unusually large stellar velocity rotation ($\approx 200 \text{ km s}^{-1}$) for the assumed inclination of the galaxy ($i \sim 30^\circ$). It also shows a very high central velocity dispersion ($\approx 214 \text{ km s}^{-1}$) that decreases drastically within the inner kiloparsec. The dispersion map reveals an extraordinary “hot” centre embedded in a significantly colder component, i.e. the disk, with no

distinct kinematic signature of the inner ring. The h_3 values anti-correlate strongly with the velocity values and so does the h_4 moment with the stellar velocity dispersion. The fact that both h_3 and h_4 values are high in the inner ring region supports the distinct kinematic properties of this substructure.

NGC 7552 displays a similar maximum rotation velocity to NGC 5701 within our FoV ($\approx 40 \text{ km s}^{-1}$). While also hosting a large-scale bar, the line of nodes is almost perpendicular to the bar’s position angle, thus the rotation is along the large-scale bar and less misaligned than in NGC 5701. A closer look reveals enhancements of the rotation velocity most likely related to the bar. Hence when taking the profile, we would see the predicted double-hump rotation curve (Bureau & Athanassoula 2005). A high velocity dispersion ring is clearly revealed outside the circumnuclear ring region. Towards the edges of the field, these values drop. In the h_3 map, only a slight anti-correlation with respect to the velocity field can be distinguished in the area where the circumnuclear ring is present. This anti-correlation is much more apparent in its velocity dispersion versus h_4 moment maps.

The three bulges in our sample display a wide range of kinematic features clearly associated to different photometric substructures, e.g. double-hump profiles σ predicted by simulations of barred galaxies (Bureau & Athanassoula 2005). Particularly interesting is the behaviour of the Gauss-Hermite higher order moments h_3 and h_4 , which are markedly different, for all galaxies, in those regions where we expect to find a mixture of populations. We will use this information in a follow-up paper (Cacho et al., in prep.) to extract the kinematic properties of the different stellar population components present in the centre of these galaxies.

5.2 Ionized-gas distribution and kinematics

We measured the distribution and kinematics of the following emission lines: $H\gamma$, $H\beta$, $[OIII]$ and $[NI]$. The resulting maps are presented in Fig. 3.

In NGC 5701, $[OIII]$ is the most prominent gas component. Its flux peaks in the centre and decreases outwards until it reaches the barred component. We barely detect $[NI]$ and $H\gamma$. The $H\beta$, however, shows a weak peak in the centre, compatible with the presence of nuclear spiral structure in this galaxy (Erwin & Sparke 2002). NGC 6753 shows a ring component in the Balmer lines, clearly visible in the $H\beta$ line map. The upper and lower part of the ring is strongly enhanced. The $[OIII]$ and $[NI]$ are mostly concentrated in the nucleus. NGC 7552 shows strong central emission in all probed emission lines, being strongest in $H\beta$ and $[OIII]$. The $H\beta$ map is in agreement with the $H\alpha$ and radio continuum maps of Pan et al. (2013) and Forbes et al. (1994), respectively. This comparison suggests that dust has not affected our measurements significantly. The very low $[OIII]/H\beta$ value in the central regions (≈ 0.17) confirms that ionisation is mostly triggered by star formation (e.g. Kewley et al. 2001).

In the three galaxies, gas rotation velocities are aligned to the corresponding stellar velocity field. The ionised gas exhibits a higher rotation velocity than the stars. Conversely, the gas velocity dispersions are lower than those of the stars. This behaviour is expected given that stars exhibit higher random motions than the ionised gas. More specifically for each galaxy, we find that the gas in the centre of NGC 5701 presents lower velocity dispersion values than in its outskirts, opposite to the stellar velocity dispersion. The velocity of the ionised gas in NGC 6753 is surprisingly close to that of the stellar kinematics. In NGC 7552, the gas velocity field shows the same twists observed in the HI and ^{12}CO (2-1) maps from Pan et al. (2013). The velocity dispersion are high around the inner Lindblad resonance (located at a radius of 1.7 kpc, Pan et al. 2013). This region sits just outside the circumnuclear ring, which has a radius of 0.5 kpc. The elevated dispersion values are likely due to shocks induced by the gas arriving at those locations though the dust lanes along the bar.

6 STELLAR POPULATIONS

The rich kinematical substructure found in the previous section may suggest a similar variety in the stellar populations of our galaxies. As a first test to classify them we have compared the central properties with larger samples in the well-known line-index- σ relation. This relation is well established for elliptical galaxies (e.g. Terlevich et al. 1981). In recent surveys, e.g. SAURON survey, this relation was confirmed for early type spirals (e.g. Peletier et al. 2007) and extended for late-type galaxies, which showed larger scatter (e.g. Ganda et al. 2007).

In order to check if our small sample could contain any atypical galaxy which would be unrepresentative of its type, we compared it to other measurements in the literature of similar galaxies. Figure 4 shows our measurements of central apertures (1.5 arcsec, same aperture as in Ganda et al. 2007) in comparison with those in the literature. NGC 5701, indicated by a green circle, lies on the edge between the E, S0s and Sa galaxies on the relation. Despite its large-scale bar, its central bulge parameters resemble a bulge of any early-type galaxy. NGC 6753, indicated by a yellow circle, lies exactly on the cloud of E-S0 galaxies, which may be surprising given the presence of spiral structure in the inner parts. Its centre is thus similar to classical S0/Sa type bulges. NGC 7552, shown by

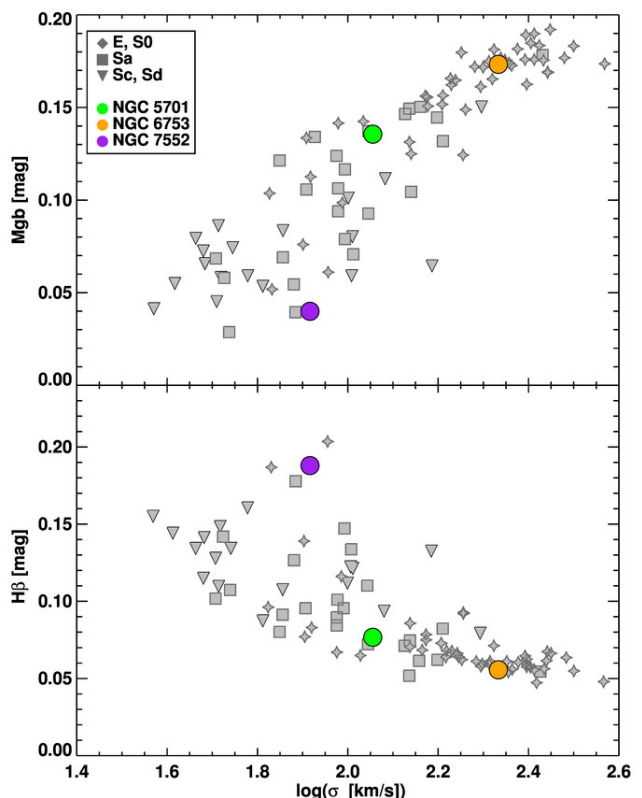


Figure 4. Line-index- σ relations for our sample of galaxies. Central aperture measurements of all three bulges (coloured circles) are compared to values from different samples (Ganda et al. 2007; Peletier et al. 2007). Values for NGC 5701, NGC 6753 and NGC 7552 are represented by green, yellow and purple solid circles respectively. Grey symbols show literature values. The upper panel shows the Mgb , expressed in magnitudes, against central velocity dispersion, while the lower panel shows the central $H\beta$, also expressed in magnitudes, against velocity dispersion. For our datapoints, we have followed the conversions from \AA to mag described in Kuntschner et al. (2006).

the purple circle, follows the behaviour of late-type galaxies, likely due to the prominent central starburst. Our sample of bulges contains, at least in their central stellar content, examples of the wide population of nearby galaxies.

6.1 Classical index-index diagrams

Figure 5 presents the measurements of absorption line strengths in index-index diagrams. The top row displays the line-strength index maps for each galaxy: $H\beta_o$, as an age indicator, and Mgb and $Fe5270$ as proxies for metallicity. In the second row, we plot $H\beta_o$ against the combined index of magnesium and iron, $[MgFe]'$ (using Mgb , $Fe5270$ and $Fe5335$, see § 4.3), and overplot a grid of MILES single stellar population models for Kroupa IMF.

NGC 5701 appears to be the oldest galaxy of the three, with a large scatter in age - from about 3 Gyr to 15 Gyr - at almost all radii. The error bar does not account for this observed spread, but the overlapping structures of bulge, bar and disk might lead to this variation. While this age spread seems to be independent of radius, the metallicity of the stars is clearly higher towards the centre, even considering the error bar. In NGC 6753, we find a steep gradient in age from the very central parts towards the ring (green points)

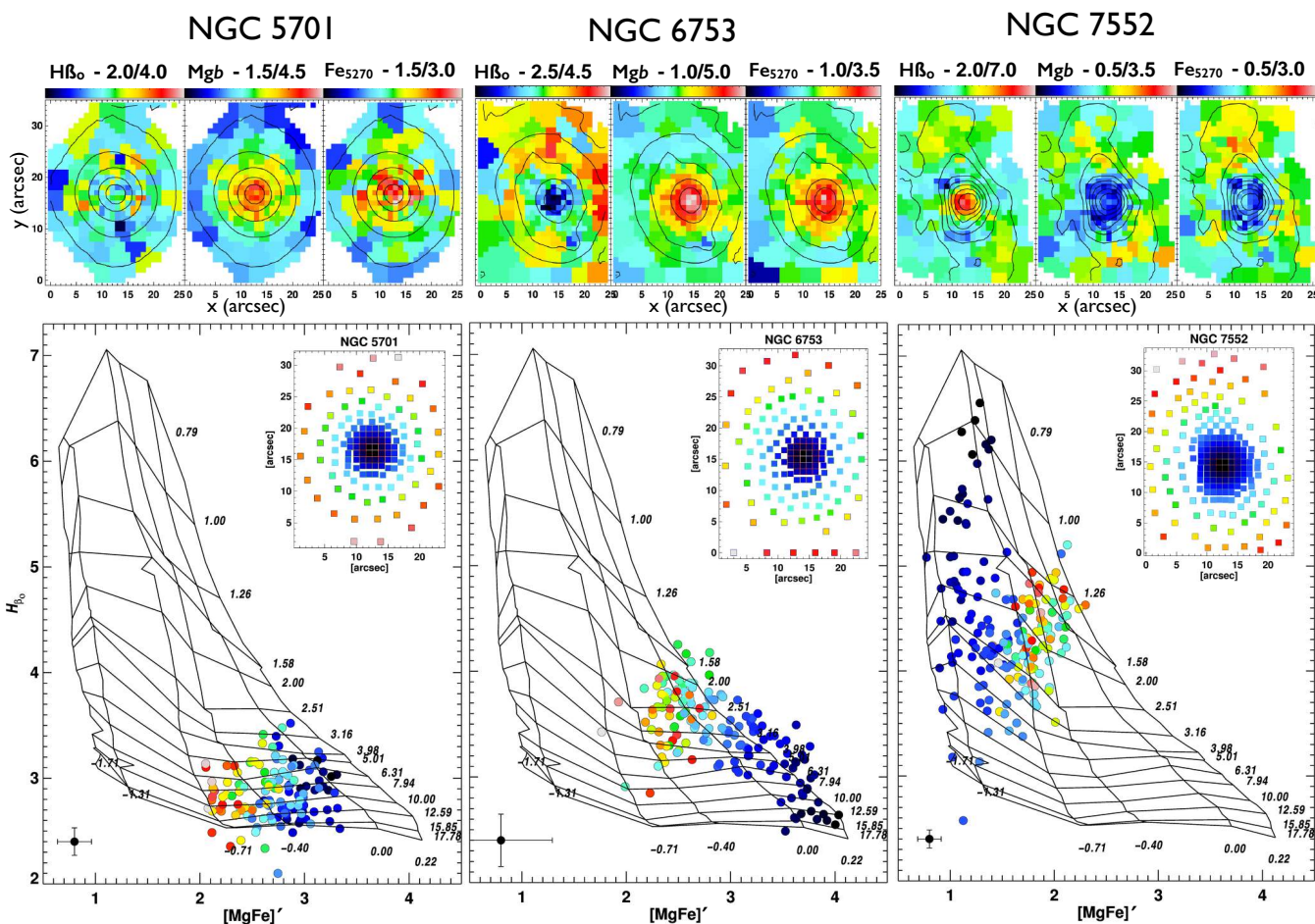


Figure 5. *Top row:* Maps of absorption line strengths for $H\beta_o$, $Mg b$ and $Fe5270$. *Bottom row:* $H\beta_o$, an age discriminator, versus the combined index of $[Mg/Fe]'$, indicating metallicities for the galaxies NGC 5701, NGC 6753 and NGC 7552, from left to right. Overplotted is a model grid of single stellar populations, roughly indicating the ages and metallicities (shown on the side of this grid). The points are colour-coded depending on their distance to the centre of the galaxy and the map in the top right corners of each panel indicates their position. In the left lower corner we indicate the typical uncertainty (weighted mean of individual errors) of the points with representative error bars.

and then an almost flat behaviour until the edges of the field. The galaxy hosts an old metal-rich population in the centre, but as soon as we enter the region dominated by the circumnuclear ring, those measurement points decrease excessively in age and most importantly fall outside of the model grid. NGC 7552 shows the opposite behaviour in the age of the central population. The central component is very young, as expected in a starburst galaxy. The known inner ring (of about 5 arcsec radius) is so small that we cannot distinguish it from the centre. It is interesting to note two low $H\beta_o$ regions above and below the centre. These locations correspond to the contact point of the gas and dust lanes with the inner ring. While the low values can be the result of dust affecting our measurements, it is also possible, as observed by e.g. Böker et al. (2008), that star formation is suppressed in those contact points and only enhanced once the gas enters the ring.

This classical approach of measuring stellar population parameters, while in principle valid for some of the regions in our galaxies, presents a number of important shortcomings. The most notable is the surprisingly large number of points in NGC 6753 that fall outside the grid. As we demonstrate in Appendix B, this is likely due to the complex mixture of populations present in those regions. This kind of bias makes it impossible to determine accurately stel-

lar population parameters such as $[Mg/Fe]$ in many locations of our galaxies. $[Mg/Fe]$ is particularly interesting as it serves as a chemical clock to establish the speed of a star formation event (i.e. being higher for quick star formation episodes). In the remaining of this paper we will only determine and use the information provided by this ratio in areas which are mostly dominated by a single stellar population (see Sec. 7 for its determination).

6.2 Radial stellar populations from full-spectral fitting

We obtained ages and metallicities with *rmodel* from the indices as well as luminosity- and mass-weighted values from the full-spectral fitting with STECKMAP. For simplicity, given that the index results are similar to the light-weighted results, in this section we only present the radial profiles of the mean stellar age and metallicity measured with STECKMAP. In Fig. 6, we plot the mean stellar age and metallicity trends (both luminosity- and mass-weighted) together with the cloud of individual values in our maps. The relations are computed as the median of the individual values found in every Voronoi bin over 1 arcsec annuli. The $[M/H]$ is determined from the metallicity values that STECKMAP gives using a solar metallicity reference of $Z_{\odot}=0.02$.

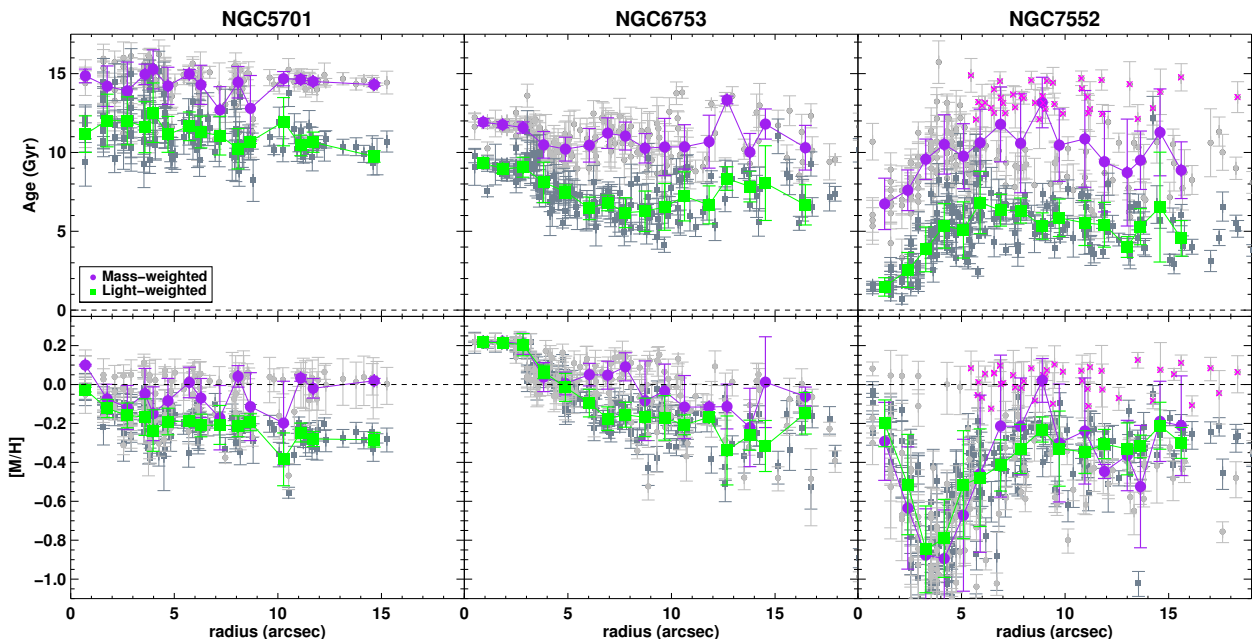


Figure 6. Stellar age and metallicity profiles for all three galaxies obtained with STECKMAP. The first row shows the age profiles. In the second row the metallicity trends. The luminosity-weighted values (green, with individual points in dark grey) and mass-weighted values (purple, with individual points in light grey) are overplotted. Errors were computed through Monte Carlo simulations. A cloud of interesting individual points for M-weighted results in NGC 7552 is marked by pink crosses (see text for details).

We calculated the uncertainties in the parameters through a series of 25 Monte Carlo (MC) simulations. We tested the difference of 25 versus 250 MC simulations and found the resulting errors to be the same within 1-2% difference. In detail, the MC procedure employed is as follows: once the best fit for the best age and metallicity values is obtained, we create 25 mock spectra by adding noise to this best fit matching the S/N of the observed spectrum. Then we run STECKMAP on those mock spectra using flat first guesses for the Stellar Age Distribution (SAD). The age (metallicity) error is the standard deviation of the ages (metallicities) of the mock fits. NGC 5701 displays a rather flat age profile, both luminosity- and mass-weighted. The metallicity profile goes from solar to sub-solar values (for the luminosity-weighted values) from the centre to the outer parts. As expected, the luminosity-weighted trends found here are quite similar to the ones obtained via line-strength indices (compare with the index values, Fig. 5). The comparison of those trends with the mass-weighted results suggests a uniform stellar distribution in the field of view of our data. Particularly interesting is the difference between the luminosity- and mass-weighted results in the very centre: the mass-weighted age being high, whereas the luminosity-weighted age shows a slight drop. The decrease in age could be due to the nuclear spiral structure present in that region.

NGC 6753 shows a much richer behaviour, suggesting a more complex stellar content. This galaxy contains a circumnuclear ring of young stars between 5 arcsec and 10 arcsec. The centre of this galaxy is quite old (both in the L- and M-weighted sense). The M-weighted age profile is flatter than the L-weighted. The metallicity profile saturates at the centre (i.e. 0.22 is the most metal-rich population in the MILES models) and shows a steep negative gradient until it reaches the ring, where the profile flattens ($[M/H] \sim -0.2$ for the L-weighted and solar values for the M-weighted profiles). The apparent broadening of the lines due to the very high central velocity dispersion did not exacerbate the STECKMAP results, since

the kinematics are given by ppxf and the resulting fits are very reasonable.

Young stars (~ 1 Gyr) are found at the centre of NGC 7552, followed by a sudden increase in age until ~ 6 arcsec where the profile appears to flatten. The M-weighted age profile behaves similarly, but does not show such young populations in the nuclear region. The L-weighted (M-weighted) metallicity in the centre of this galaxy is below solar followed by a sudden drop to a value of $[M/H] \approx -1.0$, followed by another gradual increase towards $[M/H] \approx -0.2$ values up until ~ 8 arcsec, from where it stays constant. The young and metal-rich stars that we find in the centre of this galaxy are consistent with the central starburst reported for this galaxy (Forbes, Kotilainen & Moorwood 1994; Schinnerer et al. 1997; Pan et al. 2013). Outside the inner 5 arcsec, the galaxy displays values similar to those of NGC 5701 and NGC 6753 at the same radii. Our mass-weighted profile shows an interesting feature both in age and metallicity: a separate cloud of points older than 12 Gyr and around $[M/H]=0.0$ dex values at radii larger than 5 arcsec (marked with pink crosses in the figure). We investigated the location of these bins in our maps and they belong to regions in the ring where the velocity dispersion is large (see Fig. 2) and hence might represent a distinct population with clearly different kinematics.

Two of our three galaxies host known circumnuclear star-forming rings and therefore the presence of the young stars detected from our data is not unexpected. The current analysis so far has focused in average luminosity- or mass-weighted quantities and therefore do not necessarily reveal, specially in the ring-dominated regions, the presence of any underlying old stellar population. Earlier studies of the stellar populations in star-forming rings (e.g. Allard et al. 2006; van der Laan et al. 2013a) have found a non-negligible amount of old stars in the ring regions (the mass fraction of young stars in the ring is only 30-40%). In the next sec-

Table 2. Three example test results as an excerpt of our test series. Here we are using i) a constant SFR (Test example 1) ii) exponential declining SFRs (Test examples 2 and 3), producing ranges of young-intermediate-old fractions compatible with what we might expect for real galaxies. The input is given as a mass fraction and can directly be compared with the M-weighted value which we recover with STECKMAP in the same way as for our data. The SFR input is to be compared with the determined SFR and can be related to the L-weighted value.

Test	Young				Intermediate			
	Input (Mass)	Input (SFR)	M-weight	SFR	Input (Mass)	Input (SFR)	M-weight	SFR
1	0.05	0.27	0.04 ± 0.01	0.29 ± 0.04	0.44	0.53	0.40 ± 0.13	0.47 ± 0.10
2	0.00	0.00	0.00 ± 0.00	0.00 ± 0.01	0.01	0.03	0.07 ± 0.07	0.14 ± 0.12
3	0.03	0.38	0.03 ± 0.02	0.32 ± 0.06	0.26	0.32	0.27 ± 0.15	0.33 ± 0.13

Test	Old				Extra Old			
	Input (Mass)	Input (SFR)	M-weight	SFR	Input (Mass)	Input (SFR)	M-weight	SFR
1	0.13	0.07	0.12 ± 0.02	0.07 ± 0.01	0.38	0.13	0.44 ± 0.14	0.17 ± 0.08
2	0.03	0.04	0.06 ± 0.04	0.09 ± 0.04	0.96	0.93	0.87 ± 0.10	0.77 ± 0.15
3	0.13	0.06	0.15 ± 0.03	0.10 ± 0.02	0.58	0.22	0.55 ± 0.17	0.25 ± 0.12

tion we will take advantage of the possibility STECKMAP gives us to decompose the stellar populations of our bulges into their main constituents to establish the amount of old, intermediate and young populations present in them. We will use that information, together with evolutionary models, to set constraints on the level of secular versus merger driven processes taking place in our galaxies.

7 DISSECTING THE STELLAR CONTENT AND ITS IMPLICATIONS

The observational data clearly suggest the presence of different stellar populations and demonstrate their complexity likely present in general in galactic bulges when studied in great detail. With the aid of STECKMAP, we separated the different population components, both L- and M-weighted, in three age bins: young ($\lesssim 1.5$ Gyr, formation redshift $z \lesssim 0.1$), intermediate ($1.5 \text{ Gyr} \lesssim \text{intermediate} \lesssim 10 \text{ Gyr}$, $0.1 \lesssim z \lesssim 2$) and old ($\gtrsim 10 \text{ Gyr}$, $z \gtrsim 2$). A visualization on how this is achieved can be found in the appendix, section D. For the conversion between ages and formation redshift, we are using a standard Λ CDM (cold dark matter) cosmology with a Hubble constant of $H_0 = 68.14 \text{ km/s/Mpc}$ and a value of the matter density parameter of $\Omega_m = 0.3036$.

Our aim is to reveal their spatial distribution within the galactic bulges and understand how different star formation epochs (associated to the distinct age cuts) influenced the evolutionary histories of these galaxies. The review on cosmic SFH (Madau & Dickinson 2014) summarizes distinct scenarios according to different epochs, which we will discuss more in §7.3. We are conscious about the oldest age of SSP models exceeding the age of the universe. This has been detected in former studies (e.g. Vazdekis et al. 2001) and is mainly due to degeneracies (age, metallicity, IMF, etc.) in old systems and using these models does not change the cosmology.

We acknowledge the increasing difficulty of separating intermediate and old stellar populations, but STECKMAP has been extensively tested in different works (Ocvirk et al. 2006a,b; Ocvirk, Peletier & Lançon 2008; Koleva et al. 2008; Sánchez-Blázquez et al. 2011; Koleva et al. 2011). The strategy and set of parameters used in this paper while running STECKMAP are the result of a series of tests following different schemes by different groups and by our own (e.g. Sánchez-Blázquez et al. 2014). Furthermore we point out that the age cuts are an orientation and should be taken as an age range rather than a clear cut.

Additionally, we performed our own test series using combinations of model spectra according to our age cuts and recovered

their L- and M-weighted age fractions within our proposed cuts with STECKMAP. Table 2 shows the quantitative results for three tests, the first using a constant SFR and the second and third using exponential SFRs. We also tested a combination of bursts using inputs similar to the mass fractions we obtained for the galaxies and also recovered those inputs. In all cases we see that a negligible mass of young population still causes an appreciable fraction in light, while the intermediate and old component are more dominant in mass. In fact if the mass of this young component is high (more than 10%), it will contribute a lot to the light and the old fraction can be underestimated (we observed this in other tests). Since the young mass fraction in none of our galaxies exceeds 4% (and this only in the centre of NGC 7552, in all the rest it is well below 1%), we assume that our measurements resemble more the test cases we show (and similar) and are therefore reliable. We point out that in the tests shown, the old population does not correspond to the entire old population (formation redshift $z \gtrsim 2$) but only the fraction until the extra old population ($z \gtrsim 4$), thus $2 < z < 4$.

7.1 Surface brightness profiles for each sub-population

From the different weights of each stellar populations given by STECKMAP, we can derive their contribution to the overall light of the galaxies. We used the reconstructed surface brightness distribution and multiply with the luminosity-weighted maps for each sub-population. The result of this exercise is shown in the form of maps and radial profiles in Fig. 7.

NGC 5701 is dominated by the light of an old stellar population, while in its outer parts, an intermediate population gains in importance. In the maps of Fig. 7, we clearly detect the contribution of the central nuclear spirals in the young component (12% of the light), while the overall luminosity profile is clearly dominated by the population formed long ago. Young populations often outshine old components, but here even though a young component exists, the old remains dominant. It is already evident that the young fraction must be negligible in mass (as we will show later).

The light of NGC 6753 originates mainly from an intermediate-age population with a significant contribution in light from an old population, mostly in the centre. As seen in the reconstructed maps, the contribution in light of the young population in the ring region is considerable (i.e. as much as the old component). At large radii no clear morphological feature can be associated to any of the populations.

NGC 7552 shows the young population as the major contribu-

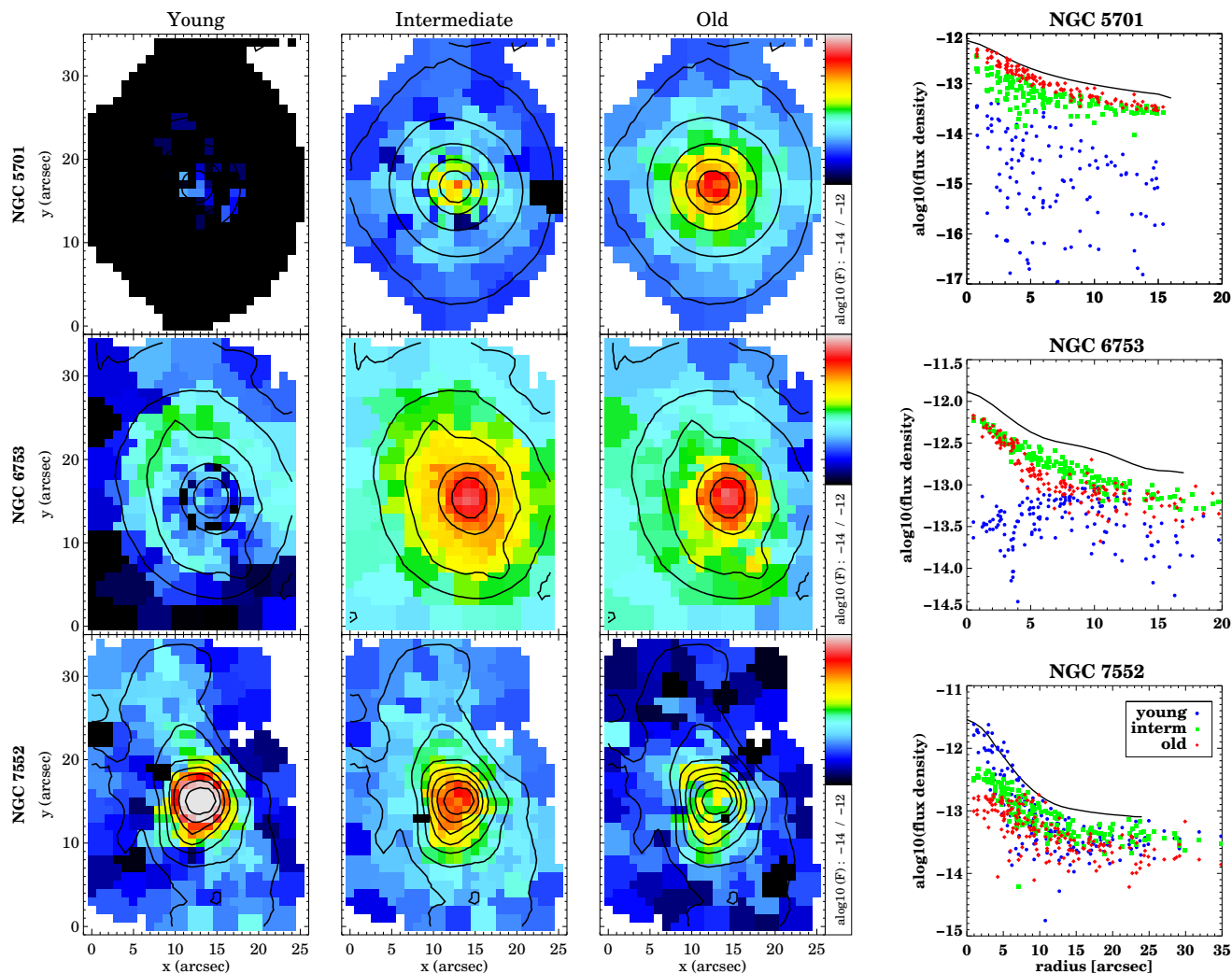


Figure 7. Surface brightness maps showing the relative contribution of young, intermediate and old stars in each spatial element throughout the galaxies and stellar luminosity profiles revealing the radial contribution of each component (young (blue circles), intermediate (green squares) and old (red diamonds)). The black line indicates an ellipse fit performed with IRAF on the intensity image obtained with WiFeS. Fluxes are given in $\text{erg s}^{-1} \text{cm}^{-2} \text{arcsec}^{-2}$ and in a logarithmic scale.

tor to the surface brightness distribution, particularly in the central region but also along the bar. The contribution of the intermediate-age population is still significant, being larger than the old component at all radii. Surprisingly a non-negligible amount of old material (almost $\sim 30\%$) is organised in a ring-like structure. This is unlike the ring in NGC 6753 where most of the material in the ring comes from an intermediate-age population. The Hubble image of NGC 7552 shows that the ring is not a closed structure, being brighter North from the nucleus. This feature is also observed in our analysis as the ring exhibits an age gradient, being younger on those regions. The young populations distributed along the bar suggests that gas must have been funnelled towards the central regions sustaining star formation over a long period.

7.2 Stellar age distributions and mass content

Figure 8 displays radial profiles of the distinct age fractions, both L- and M-weighted. We separated once more into young, intermediate and old populations, additionally indicating an even older epoch by a dashed line. The motivation of this separation remains the

same: the attempt to distinguish between different processes which according to theory happened at distinct epochs of the universe. The additional older age cut was motivated by the high mass fraction found in the former old age cut. We thus tried to constrain the formation redshift even further to compare with mass fractions proposed by cosmological models.

Here we binned the spectra in ellipses in order to raise the S/N in each of them to obtain radial SFHs and from those the distinct age fractions (a visualization of the two binning schemes can be found in the appendix, section D). The ellipticity was determined from reconstructed images directly from our WiFeS data cubes, using the IDL routine *find_galaxy.pro* written by Michele Cappellari and available as part of the *mge_fit_sectors* package⁹. Table 3 summarizes the fractions of each of these populations for the central and entire inner parts. We also point out that the L-weighted quantities here (Fig. 8) are not only obtained with a distinct binning scheme but are different measures than the computed light profiles associ-

⁹ <http://www-astro.physics.ox.ac.uk/~mxc/idl/>

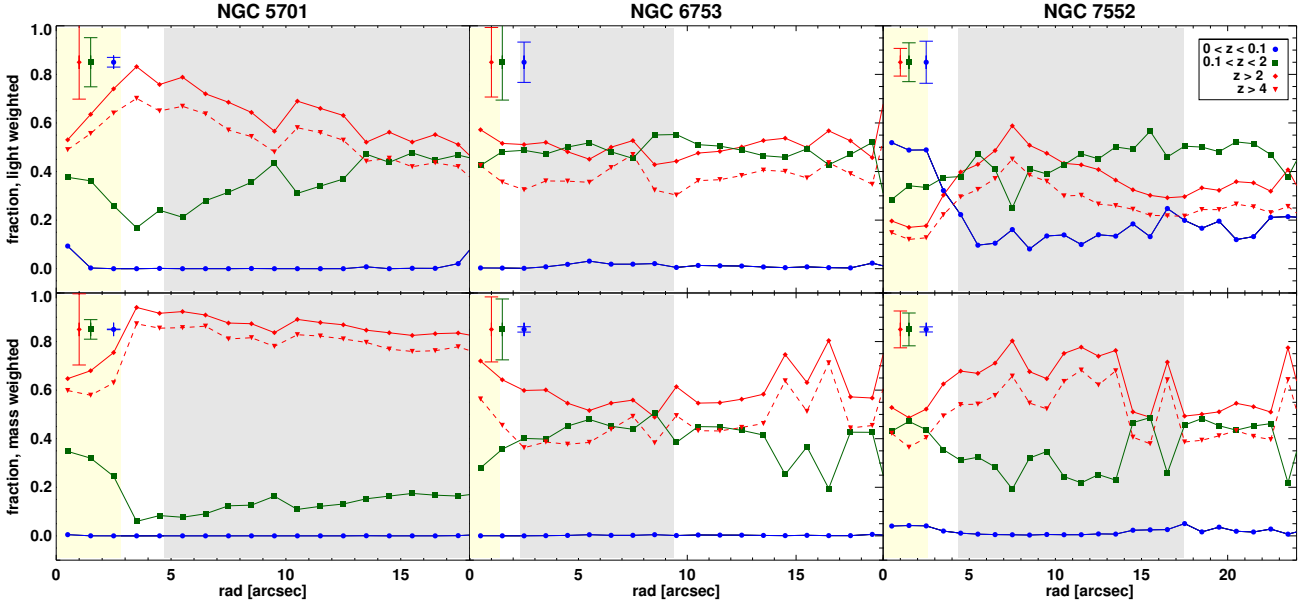


Figure 8. Fraction of young (blue dots), intermediate (green squares) and old stellar population (red rhombus, even older: red triangle and dashed line) as a function of radius. In the top left corner we indicate the corresponding uncertainties. *Top row:* L-weighted quantities; *Bottom row:* M-weighted results. Shaded regions indicate the central (< 0.3 kpc) and inner parts ($0.5 \text{ kpc} < r < 2 \text{ kpc}$) where we determine average contributions of each population (see Tab. 3).

ated to the different populations, shown in Fig. 7. Please see the visualization shown in Fig. D1 for details.

The upper panel in row 1 of Fig. 8 already reveals at first sight that the bulge of NGC 5701 is dominated by old stars throughout. These L-weighted quantities show the old centre and at around 13 arcsec, the intermediate population starts to reach the same luminosity as the old component. A slightly younger age can only be distinguished in the central 2-3 arcsec ($\sim 10\%$ in the central bin, significant enough considering the small error bar for the young population). In mass, this population of ≤ 1.4 Gyrs is negligible. This is likely the light contribution of the nuclear spiral structure. The M-weighted results show that $\sim 70\text{--}85\%$ of the stellar mass existed in fact already at $z \sim 2$. The uncertainty is large, but the fraction is significantly higher than any of the other two populations, that it comparatively dominates nevertheless. The remaining part formed from then until $z \sim 0.15$, apart from the centre which is particular. Here, in the central bin, $\sim 30\%$ is composed of the intermediate population and only $\sim 60\%$ of the old population.

NGC 6753 demonstrates subtle differences in the M- and L-weighted results. For both, old stars dominate in the centre, but less significantly in the L-weighted values. We cannot detect any young component in either. At the expected radii of the inner ring, we do not find any major difference in young or intermediate populations. Instead we measure a radially increasing amount of intermediate populations in mass from the centre which stabilizes around 10 arcsec, and remains high ($\sim 40\%$ in mass). Already in the color profile obtained by Li et al. (2011), no major indication of this ring was found. In Fig. 7 we clearly see that the light in the ring regions originates from the intermediate component. Hence this ring has formed between $z \sim 2$ and $z \sim 0.15$ or maybe even earlier, like other fossil rings that have been found (Erwin, Vega Beltrán & Beckman 2001). Furthermore, the fact that we do not detect a single enhanced region corresponding to the current position of the ring might mean that flocculent spiral structure has been present continuously throughout the last few Gyrs and thus has caused this uniform distribution

of intermediate populations. Similar to NGC 5701, a significant part of this galaxy ($\sim 50\text{--}70\%$) has already been in place at $z \sim 2$.

NGC 7552 shows a dominant young population in the centre, contributing $\sim 50\%$ to the luminosity-weighted values. This central starburst, related to the circumnuclear ring, was reported and investigated numerous times in the literature (e.g. Schinnerer et al. 1997; Pan et al. 2013). The light of the underlying old population is only dominant in a radius between ~ 6 and ~ 10 arcsec, corresponding once more to the region of the high velocity dispersion ring. The mass-weighted contribution is significant over the entire FoV (up to $\sim 75\%$), along with the intermediate component (around $\sim 45\%$). In these M-weighted results, we barely detect a contribution of the young population dominating the light. Along the ring of high stellar velocity dispersion (see Fig. 2, outside the circumnuclear ring), intermediate and especially old stars are the most significant. We might see an older component, corresponding to the higher velocity dispersion, whose central parts cannot be detected in light (lower σ) due to the dominant star burst. We report once more the existence of at least $\sim 50\%$ to $\sim 60\%$ of the galaxy's mass already at $z \sim 2$. We also wish to note that in this figure, the main trends are nicely revealed. However, the complexity of spiral arms, starburst, dust lanes and rich substructure probably require an even higher spatial resolution to better understand their interplay.

Our finding of a dominant old component of stars older than 10 Gyrs in all bulges is consistent with studies on the Milky Way (MW) bulge. Here, colour-magnitude diagrams and spectroscopic studies reveal that the majority of bulge stars are older than 10 Gyrs (e.g. Ortolani et al. 1995; Zoccali et al. 2006; Clarkson et al. 2008). The metal rich component of the bulge (e.g. Babusiaux et al. 2010; Johnson et al. 2011; Ness et al. 2012), shows evidence for comprising stars with a range of ages (Bensby et al. 2013). This metal rich component exhibits bar-like kinematics and could be associated with the secularly evolved MW bar and compared to the younger components that we find in NGC 5701 and NGC 7552. Similar results were also found in other external galaxies where the old population

dominates in mass and a younger population would make up only $\sim 25\%$ (e.g. MacArthur, González & Courteau 2009).

In all galaxies, we can see in the M-weighted results, that the mass gain in $2 < z < 4$ (difference of continuous and dashed red line) appears to be rather homogeneous radially, while the green curve resembles the distribution of young ages in the L-weighted values. This might be a hint to redistribution of material over a longer time, i.e. the slightly older stars are by now well-distributed, while the intermediate component has formed according to similar processes as the youngest component is forming now. Especially in the two barred galaxies, it is evident to see that in the last few Gyrs ($0.1 < z < 2$), a central component has formed. In both cases, this causes a rise of up to $\sim 40\%$ of the central mass. The barred structure could be responsible for driving the necessary fuel towards the centres of these galaxies in order to aliment this star formation episode. From theoretical studies we know that bars are able to remove angular momentum from the gas, driving it to the centre and enabling star formation (e.g. Combes & Sanders 1981). We cannot identify such a central structure in NGC 6753, the unbarred galaxy in our sample. The absence of this clear central component in the $0.1 < z < 2$ population supports the above scenario of the bar influence in the other two galaxies. We also detect a stronger and more confined central increase in intermediate populations for NGC 5701 than for NGC 7552. This could be an indicator that in NGC 5701, secular processes have already started earlier, in concordance with this galaxy being an earlier type.

It is common practice to calculate the Mg over Fe abundance ratio as a measure of the formation time scales of stellar populations (e.g. Thomas, Maraston & Bender 2003). It would be optimal to add this parameter to the models which are used for full-spectral fitting. However, they are not yet available. We therefore calculate it from the index-index diagrams, as it is widely done in the literature. As shown before, this value is only representative when dealing with one single prominent population. In Fig. 8, we detect in most cases a mixture of populations. We decided to determine the Mg over Fe abundance ratio only for NGC 5701 and the center of NGC 6753 based on a dominant fraction of one population (please see Appendix C for illustrations and more details). The central values result to be very high for both, ≈ 0.25 for NGC 5701 and ≈ 0.2 for NGC 6753, indicating a very rapid formation in both cases. Towards the edges of the FoV, this value decreases. This scenario is consistent with the inside-out-growth model for galaxies where the inner parts formed before and faster than the outer parts. It also fits the picture of spatially preserved downsizing presented by e.g. Pérez et al. (2013), stating that the inner regions in more massive galaxies grow faster than the outer ones. So far, former studies found increased metallicity and lower $[\alpha/\text{Fe}]$ values in the central parts of external, but also in the Milky Way bulge (e.g. Jablonka, Gorgas & Goudfrooij 2007; Moorthy & Holtzman 2006), while others detect a variety of different gradients (MacArthur, González & Courteau 2009). In our study we find elevated central $[\alpha/\text{Fe}]$ in combination with a high metallicity.

7.3 Implications for bulge evolution models

Despite the small number of galaxies investigated, our analysis allows to help putting constraints on theoretical models, trying to understand the build-up and evolution of galactic bulges as: 1) we selected a representative of early and late-type spirals which seem to exhibit the typical characteristics (see Fig. 4) and 2) we find common results within the three galaxies hinting towards a similar origin and fundamental evolution process, across these types.

In particular, we tried to get a handle on radial stellar mass distributions in the present day Universe. Despite the differences of the three investigated bulges, we find a significant amount of old stars at all radii. Hence, at least 50% of the stellar mass was already formed at $z = 2$ and even $z = 4$ (with increasing percentage from NGC 7552 to NGC 5701 where we find more than 80%). Furthermore, we detect a significant fraction of mass in a second star formation episode below $z=2$. Its present day distribution is more localized and can be associated with current morphological features such as bars.

A wealth of numerical models have already explored the early formation of galaxies and their central components. The main catalysts for the first stellar formation periods have been identified as mergers (e.g. Hernquist 1992; Bournaud, Jog & Combes 2005; Hopkins et al. 2010), the collapse itself, e.g. in the Λ CDM (White & Rees 1978), or high- z starbursts (e.g. Okamoto 2013; Finkelstein et al. 2013). Independent of the model used, the maximal percentage of bulge mass formed before $z=2$ is usually no more than 50% and often less (ranging from 10% to 50%, see also Obreja et al. 2013). Thus, the remaining mass percentage is supposed to be attributed to later evolutionary processes, related to a second star formation peak between redshift 1 and 2 (e.g. Madau et al. 1996; Norman & Spaans 1997; Spaans & Carollo 1997; Daddi et al. 2010). Nonetheless, these processes might still be one of the above, but due to lower mass densities (expansion of the universe), they are more likely of secular origin. In particular when features can be associated to morphological structures such as bars, rings, (nuclear) spiral structure etc., the likelihood of internal (and/or secular) evolution increases.

In all our galaxies we detect these different components, but we always find a higher percentage of old stellar mass than found in simulations. In the very central parts ($r < 0.3$ kpc), the old population comprises above 50% in one and around 70% in two out of the three bulges (see Tab. 3). This percentage is on average even higher (up to $\sim 85\%$) considering the inner parts ($0.5 \text{ kpc} < r < 2 \text{ kpc}$). Hence, whichever process(es) were acting in the early life of our three galaxies, they must have produced more stellar mass as commonly predicted. This is however only revealed by recovering their mass-weighted results.

All galaxies also display regions of enhanced intermediate (and young) populations which can be associated to morphological structures. Therefore, we suggest that these populations are related to a secular origin. In the following we will briefly discuss each galaxy and speculate about their formation scenario, based on our results and model comparisons.

Earlier studies already report a strong influence of environment on the resulting bulge types (e.g. Kormendy et al. 2009). In high density environments mergers are more probable to occur and influence the bulge formation, leading to old elliptical-like structures. None of the investigated galaxies shows signs of recent interaction and do not have close neighbours. NGC 5701 forms part of the Virgo supercluster as a member of the Virgo III Groups. Hence, it could have suffered mergers more likely than the other two galaxies leading to the highest percentage of old stellar mass of the three, both in inner and central regions.

Both, NGC 6753 and NGC 7552 show similar percentages but different distributions of old and intermediate populations. Their morphologies could be key for this. In NGC 6753 no bar is present and we can distinguish much better the centre composed of old stars, high in L- and M-weights. Along with its kinematic properties (high stellar velocity dispersion), the centre of this galaxy could

Table 3. Light and mass fractions in % in the central (< 0.3 kpc) and inner ($0.5 \text{ kpc} < r < 2 \text{ kpc}$) parts of young (< 1.5 Gyr, redshift $z < 0.1$) intermediate ($1.5 \text{ Gyr} < \text{intermediate} < 10 \text{ Gyr}$, $0.1 < z < 2$) and old ($> 10 \text{ Gyr}$, $z > 2$) populations. Regions are indicated in Fig. 8.

Galaxy	centre (< 0.3 kpc)			inner ($0.5 \text{ kpc} < r < 2 \text{ kpc}$)		
	young	intermediate	old	young	intermediate	old
NGC 5701 - L-weights	0.15 ± 0.09	36.6 ± 3.2	63.2 ± 8.8	0.0 ± 0.0	38.9 ± 8.4	61.1 ± 9.9
NGC 6753 - L-weights	0.30 ± 0.01	42.5 ± 0.2	57.2 ± 0.2	1.8 ± 0.9	49.2 ± 3.1	49.0 ± 3.7
NGC 7552 - L-weights	48.5 ± 0.5	33.4 ± 1.7	18.1 ± 1.3	14.0 ± 4.7	44.6 ± 6.6	41.4 ± 8.5
NGC 5701 - M-weights	0.01 ± 0.01	30.6 ± 4.8	69.4 ± 4.9	0.0 ± 0.0	14.1 ± 3.2	85.9 ± 3.3
NGC 6753 - M-weights	0.03 ± 0.02	28.0 ± 0.2	72.0 ± 0.7	0.2 ± 0.2	44.7 ± 3.8	55.1 ± 4.0
NGC 7552 - M-weights	4.1 ± 0.1	43.4 ± 1.7	52.5 ± 1.9	0.6 ± 0.4	28.0 ± 8.0	71.4 ± 8.1

present the relict of a node where the first SF occurred (e.g. Obreja et al. 2013; Barro et al. 2013)

Both NGC 5701 and NGC 7552 host large-scale bars which have affected the populations formed between $z \sim 2$ and $z \sim 0.1$, during the major second star formation epoch as predicted by simulations and found observationally. Here, the central parts show an increase of these intermediate stars: between 35-50% of the mass fraction. They can be attributed to the influence of the bar affecting this population (formed between $z \sim 2$ and $z \sim 0.1$) in particular.

We speculate that all three galaxies thus suffered a common initial stage of collapse (and/or early SF), but while NGC 5701 may have been affected also by its denser environment, the other two could retain material to form more stars in later epochs. Hence, the contribution of old stars dominating in NGC 5701 might lead to the photometric classification of a "classical bulge" (Weinzirl et al. 2009), while intermediate (and young) populations are almost equally important in NGC 6753 and NGC 7552, likely resulting in a photometric "pseudo-bulge" classification in the same former work.

8 SUMMARY AND CONCLUSIONS

In this paper we present kinematic and stellar population maps of three significantly distinct bulges with the aim to quantify the importance of different populations to better constrain their evolutionary scenarios. Our data differ from most current integral field surveys, since we obtain a very high spatial (elements of $1'' \times 1''$) as well as - and especially - high spectral resolution of $R \approx 7000$. This combination allows us to study the inner regions in galaxies in great detail and carry out a comprehensive stellar population analysis using the full-spectral fitting code STECKMAP (e.g. Ocvirk et al. 2006a,b; Koleva et al. 2008; Sánchez-Blázquez et al. 2011). We employ a novel analysis method interpreting its 2D results by deriving different stellar components and their contributions to the overall mass and light profiles of the galaxy. In addition we point out clearly the limitations that a mixture of populations can cause in deriving abundance ratios using classical line-strength methods.

Analyzing the kinematics and stellar populations of the three bulges, we deduce different formation scenarios:

- NGC 5701 consists of mainly one old solar (or slightly sub solar) stellar population, where up to $\sim 80\%$ of the galaxy's mass already existed at $z \sim 4$ distributed now radially almost uniformly (in our FoV), apart from the centre. The [Mg/Fe] values confirm a fast origin. The extremely weak nuclear spiral can be detected in the higher order moment maps (h_3 , h_4) and in the stellar light contribution. Despite its stellar bar, it does not exhibit additional star for-

mation, but shows a significant amount of intermediate populations in the central 0.5 kpc. It supports inside-out growth and appears to show a classical bulge (consistent with previous photometric analyses and increased σ) which formed almost simultaneously along with the bar.

- NGC 6753 falls into three regions: the centre is old, metal-rich, with high [Mg/Fe] values, and an extremely high stellar velocity dispersion while outside of it, σ drops and we find the presence of a significant intermediate population. We also detect an inner ring in ionised gas emission, h_4 moment and light of younger/intermediate populations. Yet, the main stellar ages vary and different populations are distributed throughout our FoV, suggesting the presence of former, short lasting ring or spiral structures producing the wide age range of intermediate (above 1.5 Gyrs) stars. Nevertheless the main component in mass is composed of old (above 12 Gyrs) stars at all radii (~ 50 -60%).

- NGC 7552 shows three regions: the starburst centre/circumnuclear ring, a high stellar velocity dispersion ring and an underlying disk component. The centre is dominated by the starburst and shows a young stellar component with around solar to sub-solar metallicities. At the inner side of the ring a metal-poor, old component can be found superimposed to a younger component. The outer parts of the ring present a smooth trend towards the intermediate-to-old solar stars plus younger and less metal-rich that we find in the rest of the galaxy. The central young component, extremely dominant in light, almost does not show in the mass-weighted results demonstrating its rather recent formation. Here a significant fraction (~ 50 -60%) of the stellar mass formed again before $z \sim 4$.

We find in all cases that most of the stellar mass has been formed long ago (before $z \sim 4$) - with a tendency to decrease for later types. We also find a strong influence of the bar on the stellar component formed between $z \sim 2$ and $z \sim 0.1$.

Comparing our results with specific simulations and models, we can confirm a two-fold formation process of galactic bulges as suggested by e.g. Obreja et al. (2013): a rapid formation of an old bulge structure in the early cosmic web initiating star formation in dense nodes (with possible influence of mergers, at least in NGC 5701) and a slower formation during the high star formation period between redshifts ~ 2 and ~ 1 of a younger component. Our results do not agree with the simulations on the mass fractions found. In all our cases the mass fraction of the old stellar component is larger - more than 50% and up to 80% - than the predicted $\sim 30\%$ or maximally $\sim 50\%$, pointing to higher star formation efficiencies or distinct evolutionary processes in the past. The secularly evolved component (here: intermediate populations) account for 30-40%.

The limitations of our sample not only concerning its size, but also its mass range, are obvious and it cannot be regarded as repre-

sentative. Nevertheless, our results point towards a common conclusion, namely the formation of already higher stellar mass fractions in the early universe than currently predicted. This work calls for even more detailed studies quantifying the importance of each process - collapse, starbursts, mergers and secular - at a given point of the lifetime of a galaxy in order to fully understand its evolutionary path. We will try to take a second step in Cacho et al. (in prep), where we extend this work to separate the kinematics associated to each population in our sample of galaxies.

ACKNOWLEDGMENTS

We thank Alexandre Vazdekis for helpful suggestions, Tim de Zeeuw for a critical reading of the original version of the paper and an anonymous referee for very useful comments. MKS, RC and JFB wish to express their gratitude to the Mount Stromlo Observatory and researchers for their friendliness and support during our extended stay. MKS acknowledges the support of the Instituto de Astrofísica de Canarias via an Astrophysicist Resident fellowship and Ignacio Martín-Navarro, Andra Stroe and Stéphane Courteau for useful discussions. RC acknowledges the Ministerio de Ciencia e Innovación by means of their FPI program (grant AYA-2010-21322-C03-03 and AYA-2013-48226-C3-3-P). JFB acknowledges support from the Ramón y Cajal Program and from the FP7 Marie Curie Actions of the European Commission, via the Initial Training Network DAGAL under REA grant agreement number 289313. TRL thanks the support of the Spanish Ministerio de Educación, Cultura y Deporte by means of the FPU fellowship. This research has been supported by the Spanish Ministry of Economy and Competitiveness (MINECO; grants AYA2010-21322-C03-02 and AYA2009-11137) and by the Spanish Ministry of Science and Innovation (MICINN; grants AYA2011-24728 and Consolider-Ingenio CSD2010-00064) and by the Junta de Andalucía (FQM-108).

REFERENCES

Allard E. L., Knapen J. H., Peletier R. F., Sarzi M., 2006, *MNRAS*, 371, 1087
Athanassoula E., 2005, *MNRAS*, 358, 1477
Babusiaux C. et al., 2010, *A&A*, 519, A77
Barro G. et al., 2013, *ApJ*, 765, 104
Bell E. F., de Jong R. S., 2000, *MNRAS*, 312, 497
Bensby T. et al., 2013, *A&A*, 549, A147
Böker T., Falcón-Barroso J., Schinnerer E., Knapen J. H., Ryder S., 2008, *AJ*, 135, 479
Bonatto C., Bica E., Alloin D., 1989, *A&A*, 226, 23
Bournaud F., Jog C. J., Combes F., 2005, *A&A*, 437, 69
Bureau M., Athanassoula E., 2005, *ApJ*, 626, 159
Cappellari M., Copin Y., 2003, *MNRAS*, 342, 345
Cappellari M., Emsellem E., 2004, *The Publications of the Astronomical Society of the Pacific*, 116, 138
Cappellari M. et al., 2011, *MNRAS*, 413, 813
Cardiel N., Gorgas J., Sánchez-Blázquez P., Cenarro A. J., Pedraz S., Bruzual G., Klement J., 2003, *A&A*, 409, 511
Cenarro A. J., Cardiel N., Gorgas J., Peletier R. F., Vazdekis A., Prada F., 2001a, *MNRAS*, 326, 959
Cenarro A. J., Gorgas J., Cardiel N., Pedraz S., Peletier R. F., Vazdekis A., 2001b, *MNRAS*, 326, 981
Cervantes J. L., Vazdekis A., 2009, *MNRAS*, 392, 691

Childress M. J., Vogt F. P. A., Nielsen J., Sharp R. G., 2014, *Ap&SS*, 349, 617
Cid Fernandes R., Mateus A., Sodré L., Stasińska G., Gomes J. M., 2005, *MNRAS*, 358, 363
Clarkson W. et al., 2008, *ApJ*, 684, 1110
Claussen M. J., Sahai R., 1992, *AJ*, 103, 1134
Coccato L., Morelli L., Corsini E. M., Buson L., Pizzella A., Vergani D., Bertola F., 2011, *MNRAS*, 412, L113
Coccato L., Morelli L., Pizzella A., Corsini E. M., Buson L. M., Dalla Bontà E., 2013, *A&A*, 549, A3
Combes F., Sanders R. H., 1981, *A&A*, 96, 164
Crocker D. A., Baugus P. D., Buta R., 1996, *ApJS*, 105, 353
Daddi E. et al., 2010, *ApJ*, 713, 686
Davies R. L., Sadler E. M., Peletier R. F., 1993, *MNRAS*, 262, 650
de Souza R. E., Gadotti D. A., dos Anjos S., 2004, *ApJS*, 153, 411
de Vaucouleurs G., de Vaucouleurs A., Corwin H. G., Buta R. J., Paturel G., Fouque P., 1995, *VizieR Online Data Catalog*, 7155, 0
Dopita M., Hart J., McGregor P., Oates P., Bloxham G., Jones D., 2007, *Ap&SS*, 310, 255
Dopita M. et al., 2010, *Ap&SS*, 327, 245
Durret F., Bergeron J., 1988, *A&AS*, 75, 273
Erwin P., 2004, *A&A*, 415, 941
Erwin P., Sparke L. S., 2002, *AJ*, 124, 65
Erwin P., Vega Beltrán J. C., Beckman J. E., 2001, in *Astronomical Society of the Pacific Conference Series*, Vol. 249, *The Central Kiloparsec of Starbursts and AGN: The La Palma Connection*, Knapen J. H., Beckman J. E., Shlosman I., Mahoney T. J., eds., p. 171
Faber S. M., 1973, *ApJ*, 179, 731
Falcón-Barroso J. et al., 2006, *MNRAS*, 369, 529
Feinstein C., Mendez M., Vega I., Forte J. C., 1990, *A&A*, 239, 90
Finkelstein S. L. et al., 2013, *Nature*, 502, 524
Fisher D. B., Drory N., 2011, *ApJ*, 733, L47
Forbes D. A., Kotilainen J. K., Moorwood A. F. M., 1994, *ApJ*, 433, L13
Forbes D. A., Norris R. P., Williger G. M., Smith R. C., 1994, *AJ*, 107, 984
Frebel A., Simon J. D., Geha M., Willman B., 2010, *ApJ*, 708, 560
Gadotti D. A., de Souza R. E., 2003, *ApJ*, 583, L75
Gadotti D. A., de Souza R. E., 2006, *ApJS*, 163, 270
Ganda K., Falcón-Barroso J., Peletier R. F., Cappellari M., Emsellem E., McDermid R. M., de Zeeuw P. T., Carollo C. M., 2006, *MNRAS*, 367, 46
Ganda K. et al., 2007, *MNRAS*, 380, 506
Gerhard O. E., 1993, *MNRAS*, 265, 213
Hameed S., Devereux N., 1999, *AJ*, 118, 730
Hernquist L., 1990, *ApJ*, 356, 359
Hernquist L., 1992, *ApJ*, 400, 460
Ho L. C., Li Z.-Y., Barth A. J., Seigar M. S., Peng C. Y., 2011, *ApJS*, 197, 21
Hopkins P. F. et al., 2010, *ApJ*, 715, 202
Jablonka P., Gorgas J., Goudfrooij P., 2007, *A&A*, 474, 763
Johnson C. I., Rich R. M., Fulbright J. P., Valenti E., McWilliam A., 2011, *ApJ*, 732, 108
Johnston E. J., Merrifield M. R., Aragón-Salamanca A., Cappellari M., 2013, *MNRAS*, 428, 1296
Kewley L. J., Dopita M. A., Sutherland R. S., Heisler C. A., Trevena J., 2001, *ApJ*, 556, 121
Koleva M., Prugniel P., Bouchard A., Wu Y., 2009, *A&A*, 501, 1269

- Koleva M., Prugniel P., de Rijcke S., Zeilinger W. W., 2011, *MNRAS*, 417, 1643
- Koleva M., Prugniel P., Ocvirk P., Le Borgne D., Soubiran C., 2008, *MNRAS*, 385, 1998
- Kormendy J., Fisher D. B., Cornell M. E., Bender R., 2009, *ApJS*, 182, 216
- Kormendy J., Kennicutt, Jr. R. C., 2004, *Annual Review of Astronomy & Astrophysics*, 42, 603
- Kroupa P., 2001, *MNRAS*, 322, 231
- Kuntschner H., 2000, *MNRAS*, 315, 184
- Kuntschner H. et al., 2006, *MNRAS*, 369, 497
- Laurikainen E., Salo H., Buta R., Knapen J. H., 2007, *MNRAS*, 381, 401
- Le Borgne D., Rocca-Volmerange B., Prugniel P., Lançon A., Fioc M., Soubiran C., 2004, *A&A*, 425, 881
- Le Borgne J.-F. et al., 2003, *A&A*, 402, 433
- Li Z.-Y., Ho L. C., Barth A. J., Peng C. Y., 2011, *ApJS*, 197, 22
- Lisker T., Debattista V. P., Ferreras I., Erwin P., 2006, *MNRAS*, 370, 477
- MacArthur L. A., Courteau S., Bell E., Holtzman J. A., 2004, *ApJS*, 152, 175
- MacArthur L. A., González J. J., Courteau S., 2009, *MNRAS*, 395, 28
- Madau P., Dickinson M., 2014, *ARA&A*, 52, 415
- Madau P., Ferguson H. C., Dickinson M. E., Giavalisco M., Steidel C. C., Fruchter A., 1996, *MNRAS*, 283, 1388
- Maraston C., Strömbäck G., 2011, *MNRAS*, 418, 2785
- Moorthy B. K., Holtzman J. A., 2006, *MNRAS*, 371, 583
- Morelli L. et al., 2008, *MNRAS*, 389, 341
- Muñoz-Mateos J. C., Gil de Paz A., Boissier S., Zamorano J., Jarrett T., Gallego J., Madore B. F., 2007, *ApJ*, 658, 1006
- Ness M. et al., 2012, *ApJ*, 756, 22
- Norman C. A., Spaans M., 1997, *ApJ*, 480, 145
- Obreja A., Domínguez-Tenreiro R., Brook C., Martínez-Serrano F. J., Doménech-Moral M., Serna A., Mollá M., Stinson G., 2013, *ApJ*, 763, 26
- Ocvirk P., Peletier R., Lançon A., 2008, *Astronomische Nachrichten*, 329, 980
- Ocvirk P., Pichon C., Lançon A., Thiébaud E., 2006a, *MNRAS*, 365, 74
- Ocvirk P., Pichon C., Lançon A., Thiébaud E., 2006b, *MNRAS*, 365, 46
- Okamoto T., 2013, *MNRAS*, 428, 718
- Ortolani S., Renzini A., Gilmozzi R., Marconi G., Barbuy B., Bica E., Rich R. M., 1995, *Nature*, 377, 701
- Pan H.-A., Lim J., Matsushita S., Wong T., Ryder S., 2013, *ApJ*, 768, 57
- Peletier R. F. et al., 2007, *MNRAS*, 379, 445
- Pérez E. et al., 2013, *ApJ*, 764, L1
- Pérez I., Sánchez-Blázquez P., 2011, *A&A*, 529, A64
- Proctor R. N., Sansom A. E., 2002, *MNRAS*, 333, 517
- Roediger J. C., Courteau S., Sánchez-Blázquez P., McDonald M., 2012, *ApJ*, 758, 41
- Sánchez S. F., García-Lorenzo B., Jahnke K., Mediavilla E., González-Serrano J. I., Christensen L., Wisotzki L., 2006, *New Astronomy Review*, 49, 501
- Sánchez-Blázquez P., Gorgas J., Cardiel N., González J. J., 2006a, *A&A*, 457, 787
- Sánchez-Blázquez P., Ocvirk P., Gibson B. K., Pérez I., Peletier R. F., 2011, *MNRAS*, 415, 709
- Sánchez-Blázquez P. et al., 2006b, *MNRAS*, 371, 703
- Sánchez-Blázquez P., Rosales-Ortega F., Díaz A., Sánchez S. F., 2014, *MNRAS*, 437, 1534
- Sansom A. E., Proctor R. N., Reid N., 1998, in *Astronomical Society of the Pacific Conference Series*, Vol. 147, *Abundance Profiles: Diagnostic Tools for Galaxy History*, Friedli D., Edmunds M., Robert C., Drissen L., eds., p. 26
- Sarzi M. et al., 2006, *MNRAS*, 366, 1151
- Schiavon R. P., Faber S. M., Rose J. A., Castilho B. V., 2002, *ApJ*, 580, 873
- Schinnerer E., Eckart A., Quirrenbach A., Boker T., Tacconi-Garman L. E., Krabbe A., Sternberg A., 1997, *ApJ*, 488, 174
- Serra P., Trager S. C., 2007, *MNRAS*, 374, 769
- Sheth K. et al., 2010, *PASP*, 122, 1397
- Spaans M., Carollo C. M., 1997, *ApJ*, 482, L93
- Terlevich R., Davies R. L., Faber S. M., Burstein D., 1981, *MNRAS*, 196, 381
- Thomas D., Maraston C., Bender R., 2003, *MNRAS*, 343, 279
- Thomas D., Maraston C., Bender R., Mendes de Oliveira C., 2005, *ApJ*, 621, 673
- Tody D., 1993, in *Astronomical Society of the Pacific Conference Series*, Vol. 52, *Astronomical Data Analysis Software and Systems II*, Hanisch R. J., Brissenden R. J. V., Barnes J., eds., p. 173
- Tolstoy E., Hill V., Tosi M., 2009, *ARA&A*, 47, 371
- Trager S. C., Faber S. M., Worthey G., González J. J., 2000, *AJ*, 120, 165
- Trager S. C., Worthey G., Faber S. M., Burstein D., Gonzalez J. J., 1998, *VizieR Online Data Catalog*, 211, 60001
- Valdes F., Gupta R., Rose J. A., Singh H. P., Bell D. J., 2004, *ApJS*, 152, 251
- van der Laan T. P. R., Schinnerer E., Emsellem E., Hunt L. K., McDermid R. M., Liu G., 2013a, *A&A*, 551, A81
- van der Laan T. P. R. et al., 2013b, *A&A*, 556, A98
- van der Marel R. P., Franx M., 1993, *ApJ*, 407, 525
- Vazdekis A., 1999, *ApJ*, 513, 224
- Vazdekis A., Salaris M., Arimoto N., Rose J. A., 2001, *ApJ*, 549, 274
- Vazdekis A., Sánchez-Blázquez P., Falcón-Barroso J., Cenarro A. J., Beasley M. A., Cardiel N., Gorgas J., Peletier R. F., 2010, *MNRAS*, 404, 1639
- Weinzirl T., Jogee S., Khochfar S., Burkert A., Kormendy J., 2009, *ApJ*, 696, 411
- White S. D. M., Rees M. J., 1978, *MNRAS*, 183, 341
- Worthey G., Faber S. M., Gonzalez J. J., Burstein D., 1994, *ApJS*, 94, 687
- Yoachim P., Roškar R., Debattista V. P., 2012, *ApJ*, 752, 97
- Zoccali M. et al., 2006, *A&A*, 457, L1

APPENDIX A: GALAXIES

NGC 5701 is an early-type galaxy with a rather smooth bulge. According to the De Vaucouleurs Atlas Description, it shows a well-defined bar imbedded in a strong inner lens, one of the best-defined examples of this phenomenon. In the centre and bar region, this galaxy does not seem to exhibit star formation nor dust. According to Erwin & Sparke (2002), this galaxy (being part of the WIYN Sample) has no inner structures apart from a nuclear spiral. Therefore, here we expect to have one dominant old population with possibly a weak younger population in the centre. Furthermore, we can test the hypothesis brought forward by Gadotti & de Souza (2003) to be a disk-lacking galaxy.

NGC 6753 is also an early-type galaxy but with more substructure. The dominant feature here is a bright inner ring which lies at the rim of a fairly uniform inner disk zone. This inner disk zone is filled with H-alpha emission (Crocker, Baugus & Buta 1996). Outside the inner ring, a broad oval zone includes complex and partially flocculent spiral structure. Beyond the broad oval zone, a well-defined, and mostly detached outer ring is found. For this project, mostly the inner parts are of importance and here we now expect to find more substructures than in NGC 5701. In particular, we aim to detect signatures of an inner ring both in the kinematics and stellar population parameters.

NGC 7552 is mostly defined by a complex, dusty bar and is best known for its central starburst, which is associated with a nuclear ring. The bar is prominent, and numerous HII regions are scattered within the disk in an asymmetric pattern. The 1 kpc starburst ring is best visible in radio wavelengths and reveals numerous supernova remnants (Forbes et al. 1994; Forbes, Kotilainen & Moorwood 1994). Nevertheless, it does not present very strong nuclear activity which simplifies studies of the circumnuclear ring. The classification of this object seemed difficult amongst the literature: The presence of giant HII regions near the corotation radius lead Bonatto, Bica & Alloin (1989) to the conclusion to deal with an H II galaxy, whereas Durret & Bergeron (1988) classified it as a LINER due to the detection of a weak [OI] λ 6300 line. The dusty bar morphology is very unusual (the De Vaucouleurs Atlas Description). As a member of the Grus triplet, the galaxy may be affected by an interaction that has disturbed its morphology. In fact, Claussen & Sahai (1992) report high molecular gas concentrations in the centre and signatures of tidal disturbance deduced from the observed asymmetries in their CO line profiles. Additionally, Feinstein et al. (1990) discovered two weaker rings (of radii 1.9 kpc and 3.4 kpc). Hameed & Devereux (1999) investigate NGC 7552 via H α , while Forbes, Kotilainen & Moorwood (1994) focus on the ring, revealing yet another inner ring of the size of only 1 kpc in the radio. Schinnerer et al. (1997) concentrate as well on this central feature showing among others Br γ images, also tracing gas ionized by recently formed massive stars and distinguish different star formation histories (SFH) for the nucleus and the ring. Furthermore, based on NIR and HST V-band continuum maps, they postulate the existence of an inner bar located inside the nuclear ring and perpendicular to the outer east-west oriented large bar. Pan et al. (2013) discuss in detail the circumnuclear starburst ring and the related formation of dense molecular gas and stars in that region.

APPENDIX B: MODEL TESTING AS LIMITS OF LS ANALYSIS: EXAMPLE NGC 6753

In order to explain the points outside the grid for NGC 6753 seen in Fig. 5, we combined different single stellar population models,

changing their weights, ages and metallicities, similar to Fig. 8 in Kuntschner (2000). We use the same SSP MILES models which we use for the SSP grid¹⁰. From the individual spectra for a certain age and metallicity for each population, we create a final spectrum which we analyze using the same line-strengths indices routine which we apply to the galaxy spectra. When combining the spectra, we impose the contribution in light per population. In the two test cases we show here, we chose two different metallicities for the young population: 0.00 and 0.22 dex, and two ages: 1.00 Gyr and 1.26 Gyrs, and the following weighting scheme:

- 100% young stars
- 50% young and 50% old stars
- 20% young and 80% old stars
- 10% young and 90% old stars
- 5% young and 95% old stars
- 1% young and 99% old stars
- 100% old stars

Fig. B1 summarizes the test outcome when combining an old (≈ 12.5 Gyr) population with solar metallicity (left column) with the two different young populations of each two different metallicities. On the right plot, we show the same, just with the older population having super solar metallicity.

We also performed this same analysis weighing the spectra in mass. Here, it was much easier to move points outside the grid. Already very small mass fractions of a young population resulted in a point outside in the measurement of the combination. This is due to the fact that even a small fraction in mass of a young population (~ 1 -5%, depending on the exact age and its metallicity) will have a strong contribution in light and therefore outshine most of the old population. Since the index measurements are based on luminosity-weighted quantities, we foster our analysis with the L-weighted tests.

Based on these tests, we conclude that NGC 6753 presents an old, metal-rich (about solar) population, significant in mass, but whose light is mixed with a strong younger population. The old population is seen in the inner parts. Slightly further out, the young population begins to contribute more in light; according to the tests, we need approximately 20% of the light contribution coming from the young population (and only 1 to 5% in mass). Therefore, the index values that we measure move upwards and hence out of the grid. Thus, these values do not indicate a failure of our measurements, but the combination of a rather metal-rich population in combination with a low mass-fraction of young stars.

More importantly, this result implies that abundance ratios measured in the region of population mixtures will be unreliable if it is sufficiently altered by the above effect.

APPENDIX C: α - ENHANCEMENT

In Fig. C1 we present the results of the abundance ratio analysis for two of the three galaxies. On the left hand side, the abundance is plotted as a function of radius indicating the overall decline from the center to the outskirts of the two galaxies, with increasing scatter in the individual values, especially for NGC 6753. On the right, the abundance versus the age is shown with color-coded points in the same way as before: darker points are central ones and yellow, red points belong to the edges of the field.

¹⁰ <http://miles.iac.es/pages/webtools/get-spectra-for-a-sfh.php>

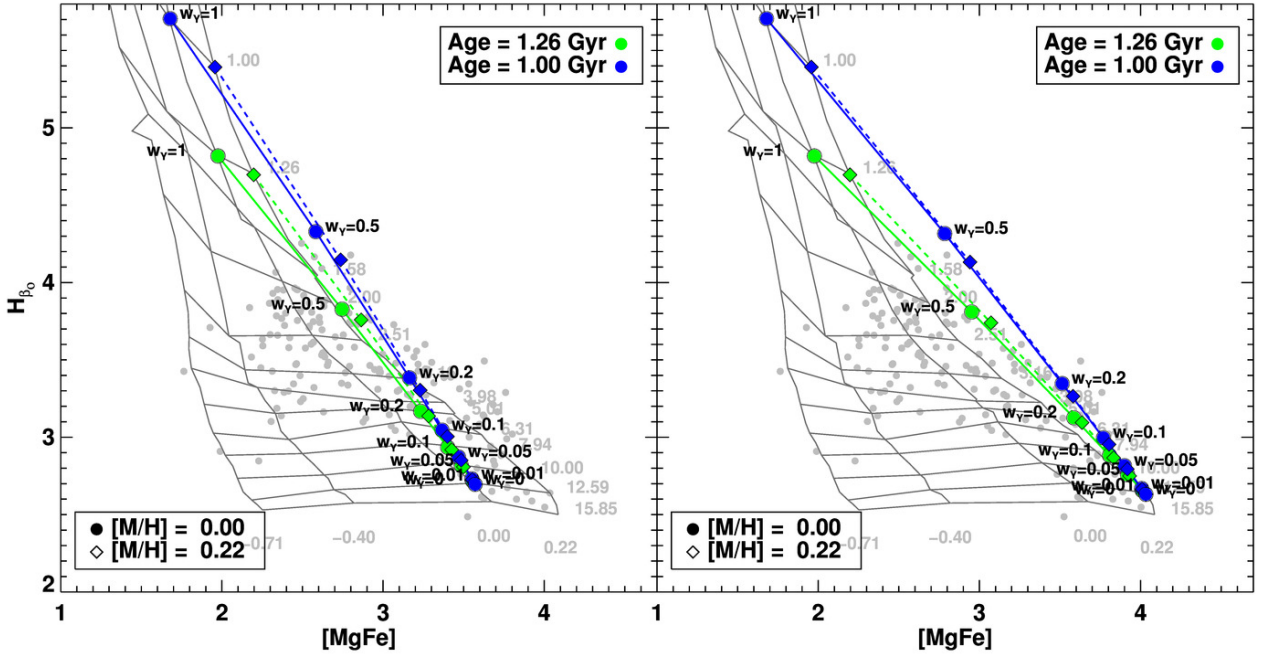


Figure B1. The influence of the combination of very different sets of stellar populations on the index results. We show model tests in colors: green and blue points indicate age, round symbols solar metallicity and rhombic symbols super solar metallicity. The different fractions of young populations are indicated next to the points, for the 1.00 Gyr population on the right, the 1.26 Gyr, on the left. In addition, we display the index measurements as obtained from NGC 6753 in grey dots. See section B for more details.

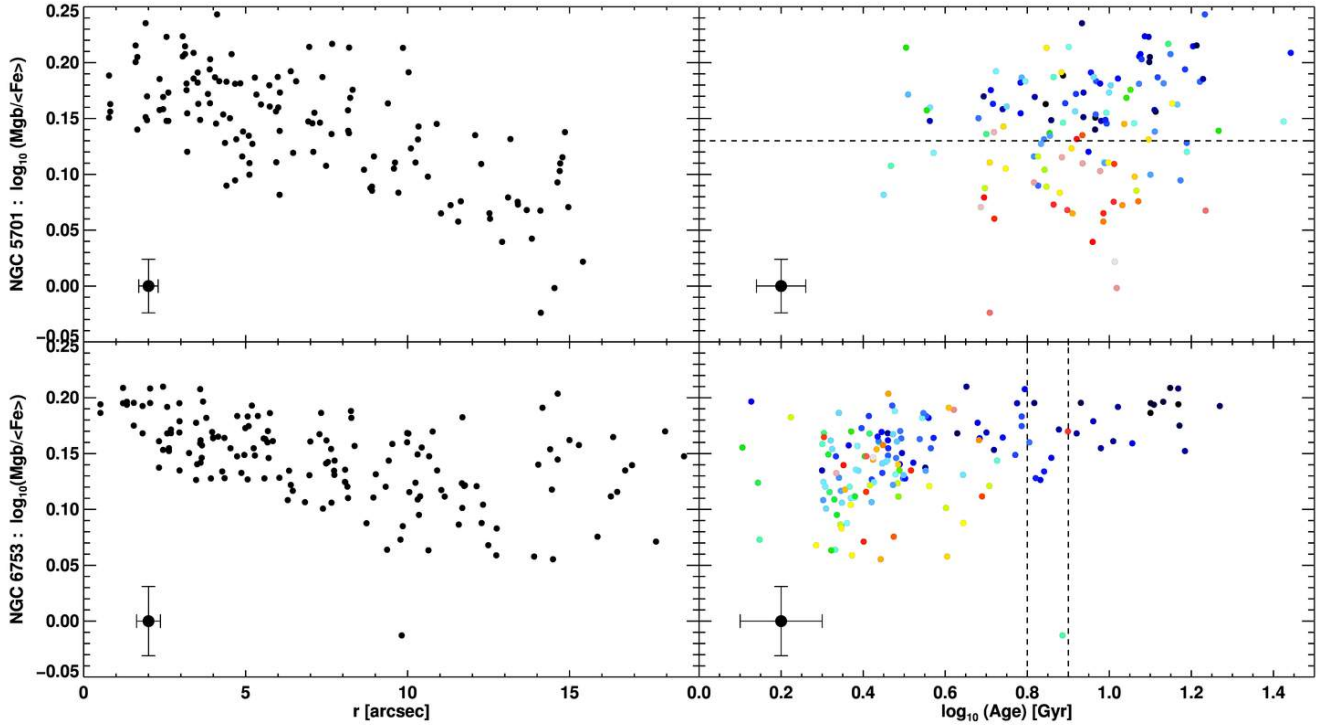


Figure C1. We show abundances as a function of radius for and age for two galaxies: upper row: NGC 5701, lower row: NGC 6753. The horizontal line indicates for NGC 5701 the separation of the central bulge and the outer bar dominated region. Vertical lines (drawn at 6.31 and 7.94 Gyrs) separate the region where the values can be trusted (right side) and where, due to an obvious mixture of populations, we cannot trust the values any longer (left side); the region in the middle could be debatable. Representative error bars are given in the left lower corners.

NGC 5701 shows a separation of two clouds indicated by the horizontal line. The ages are rather homogeneously distributed. The profile of NGC 6753 reveals certain details: going outwards, we can recognize a series of bumps. We deliberately chose to represent individual points here since averaging even in ellipses would wash out signatures of the patchy spiral structure. Comparing this profiles thus with the unsharp mask in Fig. 1, we can qualitatively correlate the wiggles in the profile with the spiral arms. Nevertheless, in this region the values cannot be fully trusted as pointed out before which might actually be the result of the wiggles. On the right, we indicate with the two vertical lines the different regions: to the right, we can trust the points. This narrow regime without too much scatter corresponds to the central part of the galaxy (those points which do not fall out of the grid in Fig. 5). In between the lines, the points start to be less reliable and to the left, we cannot fully trust them due to the mixture of different populations (the increasing scatter also hints to this problem).

APPENDIX D: AGE BINNING AND STECKMAP ANALYSIS

In Fig. D1 we illustrate the two different processes of using STECKMAP, both times departing from the WiFeS spectral cube, using the emission-cleaned spectra coming from the GANDALF analysis, shifted to rest frame according to the stellar velocity (see Sec. 4.1) and broadened to 8.4 \AA . In every case, we fix the stellar kinematics and fit exclusively for the stellar content avoiding the metallicity-velocity dispersion degeneracy (Sánchez-Blázquez et al. 2011).

Binning 1 (maps): We use this binning, a Voronoi binning over the two-dimensional maps, almost throughout our entire analysis, starting with the kinematics, then the index analysis and later the first analysis with STECKMAP. Hence, from these maps we obtain with STECKMAP light and mass weighted stellar age distributions (SAD) and from these distributions, we obtain fractions in our three (four) defined age cuts. This process of dividing the SADs into the distinct age bins is visualized in Fig. D2. As shown in Fig. D1, we do obtain at first corresponding maps for the L- and M-weighted SADs, which we don't display in this paper due to simplicity. From those, we extract the corresponding age fractions, again in maps. Multiplying the L-weighted fractions with the overall intensity, we obtain the light maps corresponding to each of the populations. Using the ellipticity, we then plot the radial profiles directly from those maps, as shown in Fig 7.

Binning 2 (ellipses): This second binning scheme is only employed in the final analysis in order to raise the S/N. Here we perform an elliptical binning prior to the STECKMAP analysis. The radially binned spectra are then analyzed with STECKMAP to produce directly radial L- and M-weighted SADs from which we extract once more the fractions of young, intermediate and old populations, as shown in Fig. 8.

Figure D2 illustrates for three example spectra (one for each galaxy) the process of obtaining the different age fractions from the SADs. On the left we show the data and STECKMAP fit and on the right the corresponding SADs, once L- and once M-weighted. On each plot, we indicate the area under the SAD curve which corresponds to the young, intermediate and old SP. The associated fractions are given on top of these areas.

APPENDIX E: COMPLETE MAPS

We show maps of the stellar and ionized-gas distribution and kinematics (from the blue grating) as well as indices from the blue and red spectra for the three galaxies of this study. First row: HST or Spitzer image, its unsharp-mask and the name, Hubble type, position, absolute B-band magnitude and inclination of the galaxy. Second row: (i) stellar mean velocity V (in km s^{-1}), (ii) stellar velocity dispersion σ (in km s^{-1}), (iii) and (iv) Gauss-Hermite moments $h3$ and $h4$. Third row: (i) $H\beta$ flux (in logarithmic scale), (ii) same for the $H\gamma$, [OIII] and [NI] line, (v) mean radial ionised gas velocity and (vi) ionised gas velocity dispersion (in km s^{-1}). Fourth row: index maps from the blue spectra for (i) $H\beta$, (ii) $H\beta_o$, (iii) Fe5015, (iv) Mg b , (v) Ca4227 and (vi) G4300. Fifth row: index maps from the blue spectra for (i) Fe4383, (ii) Fe4668, (iii) Ca4455, (iv) Fe5270, (v) Fe5335 and (vi) Fe5406. Sixth row: index maps from the red spectra for (i) CaT, (ii) CaT*, (iii) PaT, (iv) Ca1, (v) Ca2, (vi) Ca3 - as defined in Cenarro et al. (2001a). The cut levels are indicated in a box on the right-hand side of each map.

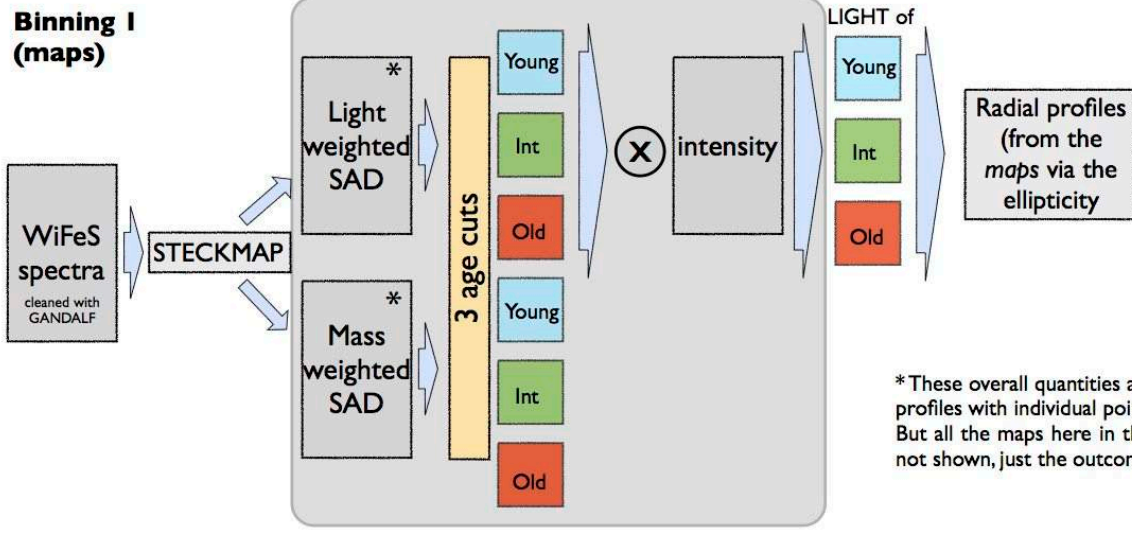
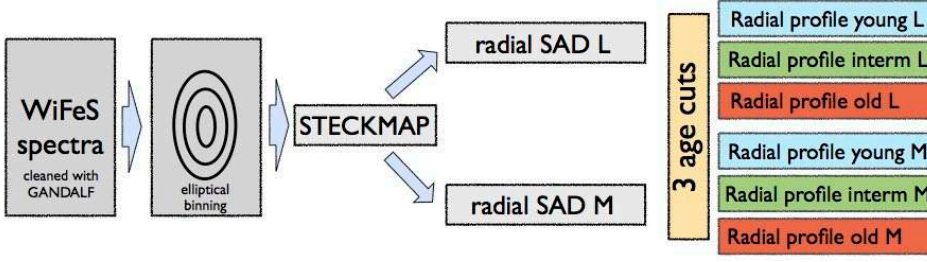
**Binning I
(maps)****Binning II
(ellipses)**

Figure D1. Visualization of the two distinct binning schemes. *Top:* Binning 1 via maps, where the grey area indicates results that we obtain during the process but do not show in the paper). The corresponding figures using this scheme are Fig. 6 and Fig. 7. *Bottom:* Binning 2 via ellipses used for the final part of our analysis, shown in Fig 8.

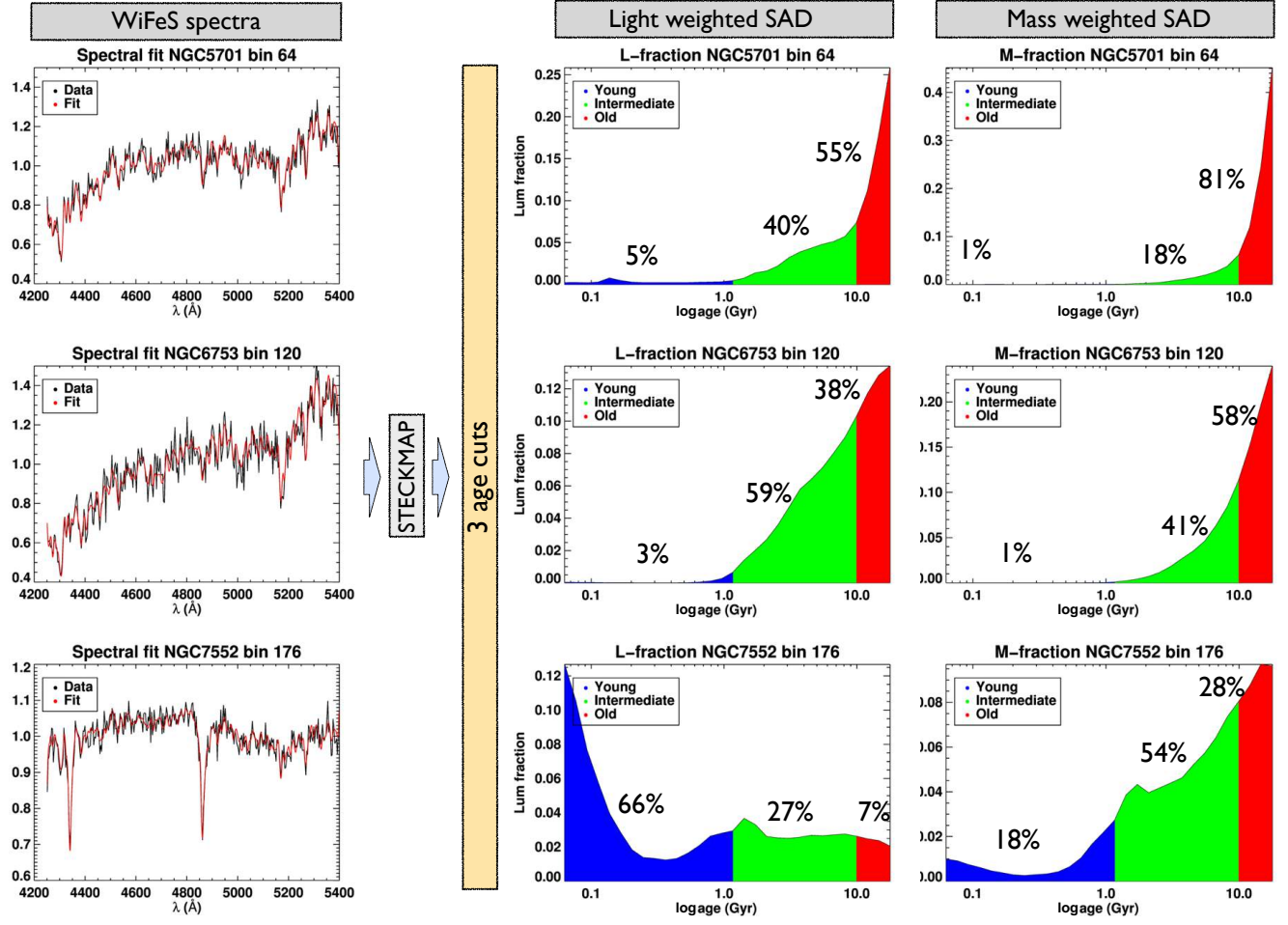


Figure D2. Visualization of the different age bins obtained from the STECKMAP SADs. *Left:* Data (black) with the STECKMAP fit (red) over plotted. *Right:* The L- and M-weighted SADs with the young (blue), intermediate (green) and old (red) (also from left to right on each plot) fractions indicated (areas under the SAD curve).

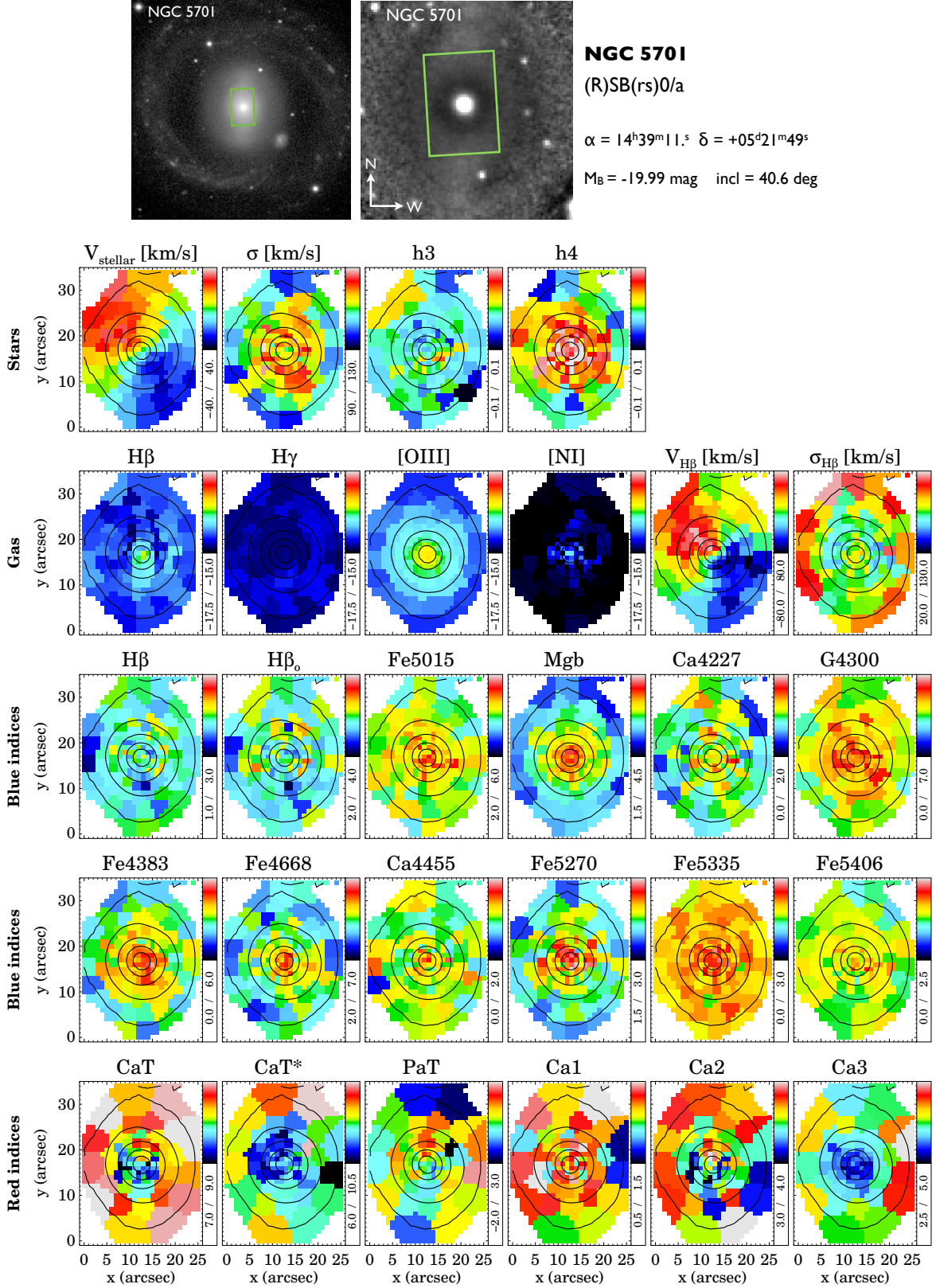


Figure E1. Summarized maps for NGC 5701 from blue and red gratings. See text for details.

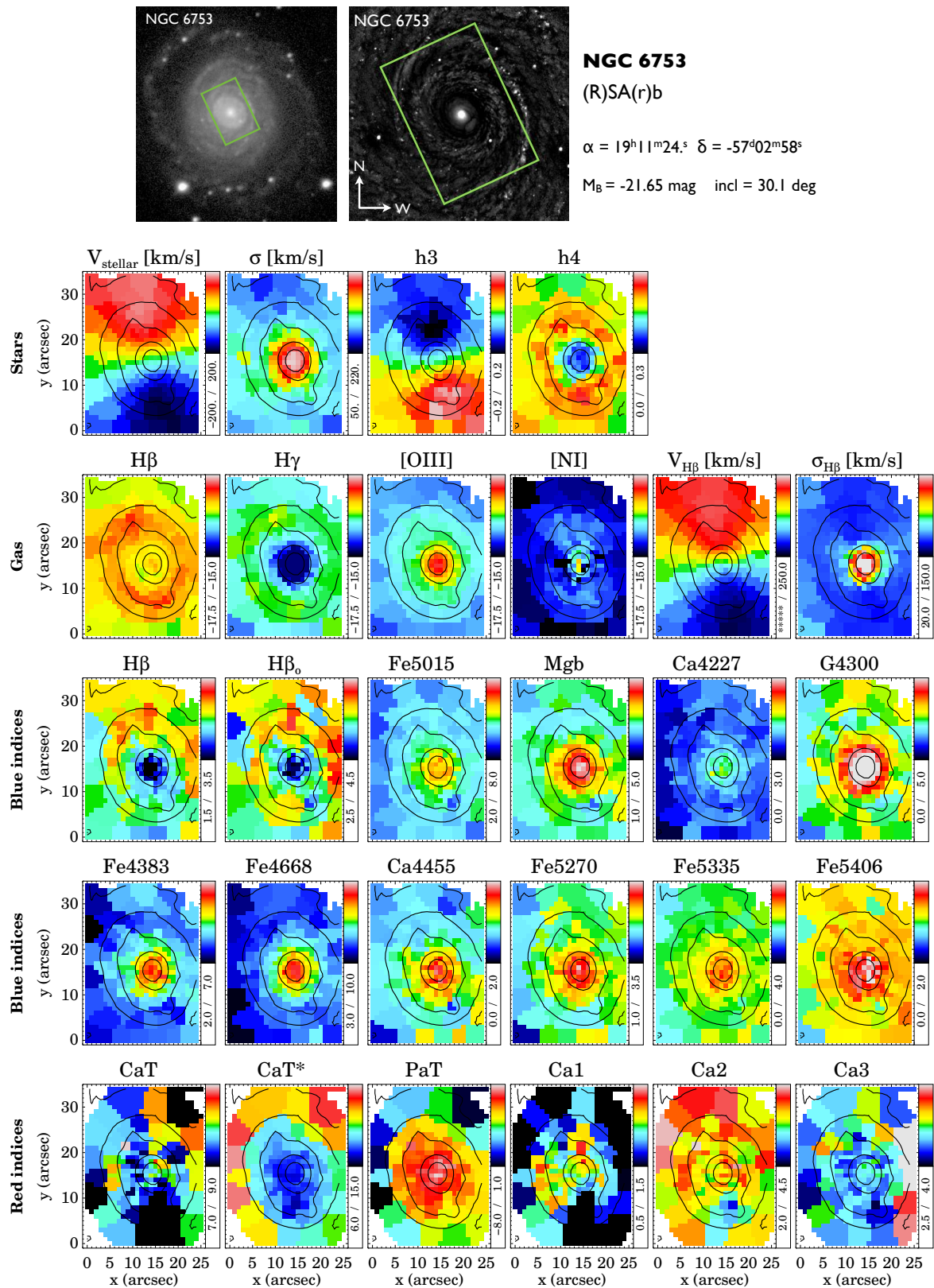


Figure E2. Summarized maps for NGC 6753 from blue and red gratings. See text for details.

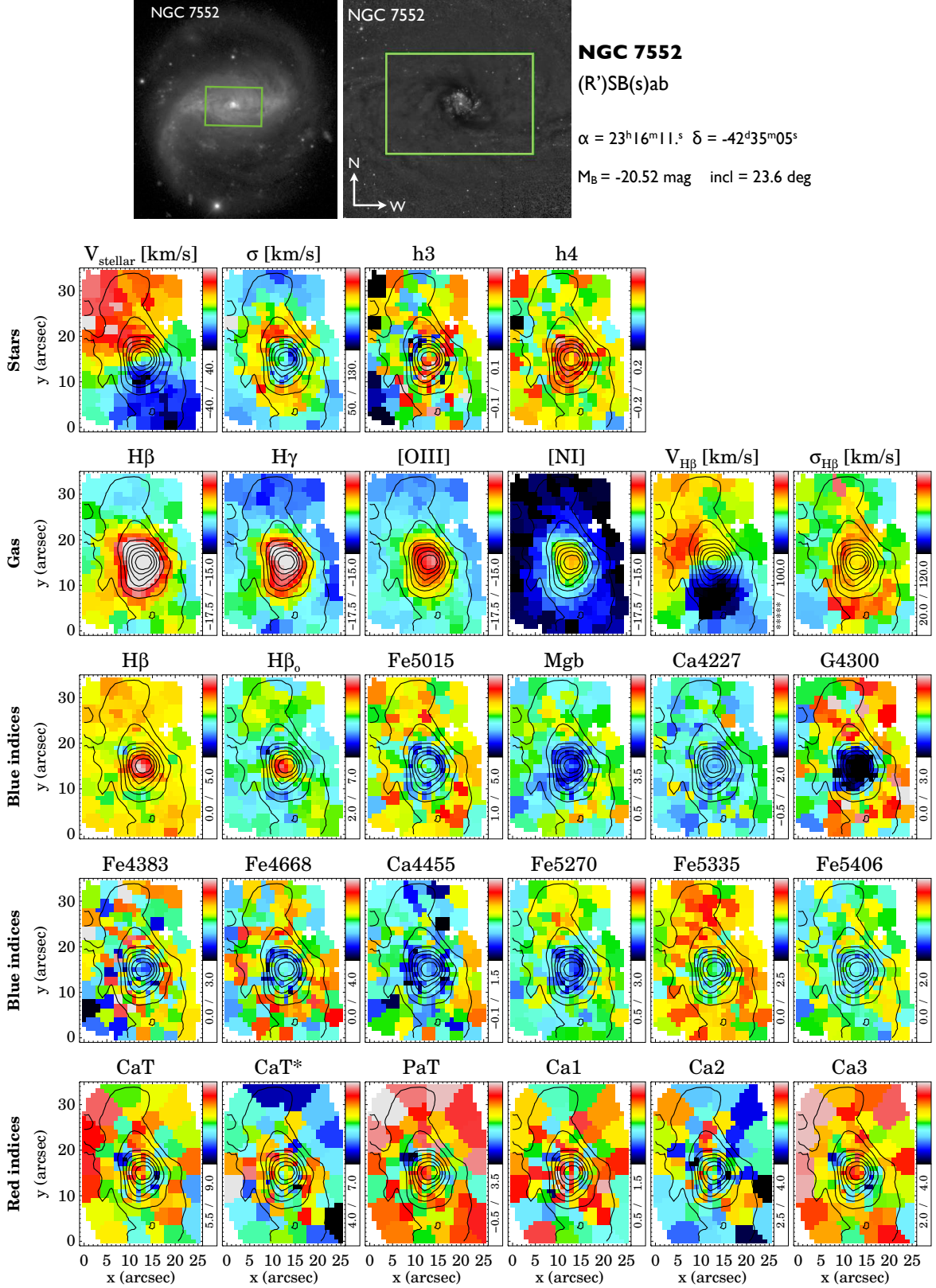


Figure E3. Summarized maps for NGC 7552 from blue and red gratings. See text for details.